AGU PUBLICATIONS

JGR

Journal of Geophysical Research: Space Physics

RESEARCH ARTICLE
10.1002/2015JA021953

Key Points:
- TEC increases with similar morphology during the positive phases of nine ionospheric storms
- TEC changes correlate with Dst better than with ap in the negative storm phase
- CMEs that interact only tangentially with Earth can nevertheless produce significant TEC changes

Supporting Information:
- Supporting Information S1
- Movie S1
- Movie S2
- Movie S3
- Movie S4
- Movie S5
- Movie S6
- Movie S7
- Movie S8
- Movie S9
- Movie S10
- Movie S11
- Movie S12
- Movie S13
- Movie S14

Correspondence to:
B. E. Wood,
brian.wood@nrl.navy.mil

Citation:
Wood, B. E., J. L. Lean, S. E. McDonald, and Y.-M. Wang (2016), Comparative ionospheric impacts and solar origins of nine strong geomagnetic storms in 2010–2015, *J. Geophys. Res. Space Physics*, *121*, 4938–4965, doi:10.1002/2015JA021953.

Received 24 SEP 2015
Accepted 24 APR 2016
Accepted article online 27 APR 2016
Published online 11 JUN 2016

Comparative ionospheric impacts and solar origins of nine strong geomagnetic storms in 2010–2015

Brian E. Wood[1], Judith L. Lean[1], Sarah E. McDonald[1], and Yi-Ming Wang[1]

[1]Space Science Division, Naval Research Laboratory, Washington, District of Columbia, USA

Abstract For nine of the strongest geomagnetic storms in solar cycle 24 we characterize, quantify, and compare the impacts on ionospheric total electron content (TEC) and the U.S. Wide Area Augmentation System (WAAS) with the heliospheric morphology and kinematics of the responsible coronal mass ejections (CMEs) and their solar source regions. Regional TEC responses to the events are similar in many respects, especially in the initial positive phase. For the subsequent negative phase, *Dst* is a better indicator than *ap* of the magnitude of the TEC decrease. The five events that arrive between 13:00 UT and 21:00 UT (local daytime in the U.S.) produce large WAAS degradations, and the four events that arrive outside this time of day produce lesser or no WAAS degradation. Our sample of geoeffective events includes CMEs with only modestly fast speeds, ones that only provided glancing impacts on Earth by their shock sheaths and ones not associated with any significant flare. While all of the CMEs traveled faster than the solar wind, they nevertheless have a wide range of velocities and produced a range of B_z values; neither speed nor B_z correlates significantly with ionospheric impact. Comparison with the locations of surface activity leads to estimates of deflection for the CMEs, with the average deflection being 19°. At least a few events may have missed Earth entirely in the absence of coronal deflection.

1. Introduction

Specifying, understanding, and forecasting eruptive solar events and their impacts on the terrestrial environment have challenged space research for more than a century, since Carrington detected a solar disturbance in September 1859 that 17.5 h later destroyed the fledgling U.S. telegraph network [*Tsurutani et al.*, 2003; *Cliver and Dietrich*, 2013]. The technological and engineered infrastructure of modern society is also susceptible to disruption by solar storms because it relies on capabilities that encounter or utilize the space environment [*National Research Council*, 2013; *Ferguson et al.*, 2015]. The ionosphere is a particularly important component of this susceptibility because fluctuations in electron density can refract, distort, and reflect radio waves that facilitate precision timing, navigation, and communication [*Cannon*, 2009]. Forecasting when and how a solar eruption might disturb the ionosphere is needed with ever increasing precision in support of these activities. Recognition of the need to specify, understand, and forecast space weather and terrestrial impacts is growing accordingly [*Royal Academy of Engineering*, 2013; *Space Weather Operations, Research, and Mitigation* (*SWORM*) *Task Force*, 2015].

Forecasting of a solar eruption's geoeffectiveness, in general, and its ionospheric impacts, in particular, has yet to achieve the skill necessary for operational utility. For example, NOAA's Space Weather Prediction Center (SWPC) initially forecast that a solar storm on 15 March 2015 would cause a G1 geomagnetic event at Earth around 17 March. This minimal impact was expected because of the glancing impact on Earth projected by the operational model that SWPC uses to estimate the velocity and density of a coronal mass ejection's transit through the heliosphere. In fact, a G4 (severe) storm manifested, beginning 15 h ahead of the forecast arrival time, causing significant ionospheric depletion and spectacular aurorae.

Ionospheric storms and aurorae have been studied extensively in recent solar cycles using both observational analysis and models but independently of their solar-heliospheric origins [e.g., *Fuller-Rowell et al.*, 1994; *Buonsanto*, 1999; *Araujo-Pradere et al.*, 2006; *Mendillo*, 2006; *Lekshmi et al.*, 2011; *Mukhtarov et al.*, 2013; *Borries et al.*, 2015]. Studies of ionospheric variability typically utilize an index of geomagnetic activity to quantify the general geoeffectiveness of the coronal mass ejection responsible for the storm. For example, the *Kp* index defines the SWPC's geomagnetic storm scale from G1 to G5, with G1 ($Kp = 5$) representing minor storm conditions and G5 ($Kp = 9$) representing an extreme storm.

Solar storms, their connections to magnetic sources in the Sun's atmosphere, and the resultant coronal mass ejections (CMEs) and interplanetary coronal mass ejections (ICMEs) observed at 1 AU have also been studied

extensively but independently of their ionospheric impacts [e.g., *Möstl et al*., 2010; *Lugaz et al*., 2012; *Davies et al*., 2013; *Kilpua et al*., 2014; *Li et al*., 2014; *Möstl et al*., 2014; *Patsourakos et al*., 2016]. These studies similarly categorize a solar storm's geoeffectiveness according to indices such as *Kp*, *ap*, and *Dst*.

The ability to specify with observations the chain of coupled processes that originates on the Sun, traverses the heliosphere, modifies Earth's space environment, and disrupts operational activities provides a stronger foundation for advancing, understanding, and forecasting behind than is possible from the study of solar and ionospheric storms independently of each other. While comprehensive databases exist of ionosphere total electron, heliospheric properties at 1 AU, and coronal conditions and have been extensively analyzed to address pieces of this chain, the full integration of an ionospheric storm's temporal evolution and morphology with its solar-heliospheric origins is possible only during the past decade, enabled by launch of the twin Solar TERrestrial RElations Observatory (STEREO) spacecraft in 2006 [*Howard et al*., 2008]. These spacecraft observe the Sun at a roughly 1 AU distance from the Sun, but at very different locations which permit them to view, from two different perspectives, the heliosphere between the Sun and Earth.

Although solar cycle 24 is less prolific in major storm production, it has nevertheless produced significant geoeffective events [*Gopalswamy et al*., 2015]. We compare and contrast a selection of nine geomagnetic storms and their solar origins seen in the first half of solar cycle 24, covering 2010–2015. We utilize ionospheric, heliospheric, and solar observations to simultaneously study the interconnectivity of these nine events, to better understand why some solar storms prove more ionospherically impactful than others and why some, but not others, impact operational activities, specifically the Wide Area Augmentation System (WAAS) that provides high precision GPS-based aviation navigation within North America.

Definitive connections between solar eruptions observed at the Sun and resulting geoeffective events at Earth are crucial for improved forecasting capability. While the nine significant events that we identify and analyze do not constitute a robust statistical study, in comparing for the first time the interconnected operational, ionospheric, heliospheric, and solar aspects, we demonstrate with this suite of events an integrated approach that may advance understanding, as future observing systems and more extensive databases allow.

2. Observations

Solar activity in cycle 24 began to increase in late 2009, following a historically long and deep solar minimum [*Lee et al*., 2009; *Russell et al*., 2010]. Compared with earlier cycles in the space era, solar cycle 24 has reached only modest activity levels; solar maximum probably occurred in 2014, when the yearly mean sunspot number peaked at a value of 79, close to the value of 78 attained at the maximum of cycle 16 in 1928.

The first significant geomagnetic storm of solar cycle 24 occurred on 5 April 2010 and was associated with a CME initiated at the Sun on 3 April 2010 [*Möstl et al*., 2010; *Rouillard et al*., 2011; *Wood et al*., 2011]. Other significant storms followed as solar activity increased to the maximum of its 11 year cycle, with 13 storms having *ap* values in the range 111 to 207. As of July 2015, none of the storms in cycle 24 rival the strengths of the largest storms in recent prior cycles, such as the Bastille day storm on 15 July 2000 and the Halloween Storm on 29 October 2003 in cycle 23, or the Quebec Blackout storm on 13 March 1989 in cycle 22, for all of which *ap* reached 400.

Figure 1 shows evolving solar activity in cycle 24 indicated by the 10.7 cm radio flux, $F_{10.7}$, and the geomagnetic activity index, *ap*, with 3 h time resolution. Magnetospheric activity indices such as *ap*, and also *Kp* and *Dst*, are common measures of the severity of a geomagnetic storm. The unitless *Kp* index is a quasi-logarithmic measure of geomagnetic variability, with a time resolution of 3 h, based on measurements from 13 locations between geomagnetic latitudes of 44 and 60° (north and south). The *Kp* index is on a scale from 0 to 9, with increments of one third allowed using a "+" or "−" to indicate ±0.3 (e.g., *Kp* = 4+ or *Kp* = 4−). The *ap* index shown in Figure 1 is a more linear version of *Kp*, with a predefined one-to-one correspondence between *Kp* and *ap*. An alternative to *Kp*/*ap* is the *Dst* ("disturbance storm time") index, quantifying the depression of the horizontal component of the geomagnetic field during geomagnetic activity from a network of monitors near the geomagnetic equator, with *Dst* typically having units of nT.

We include in our sample of geoeffective cycle 24 events the five events with the strongest degradations in WAAS coverage (24 October 2011, 26 September 2011, 5 August 2011, 27 February 2014, and 4 June 2011) and the five events with the highest *ap* values (9 March 2012, 5 April 2010, 5 August 2011, 2 October 2013, and 17 March 2015).

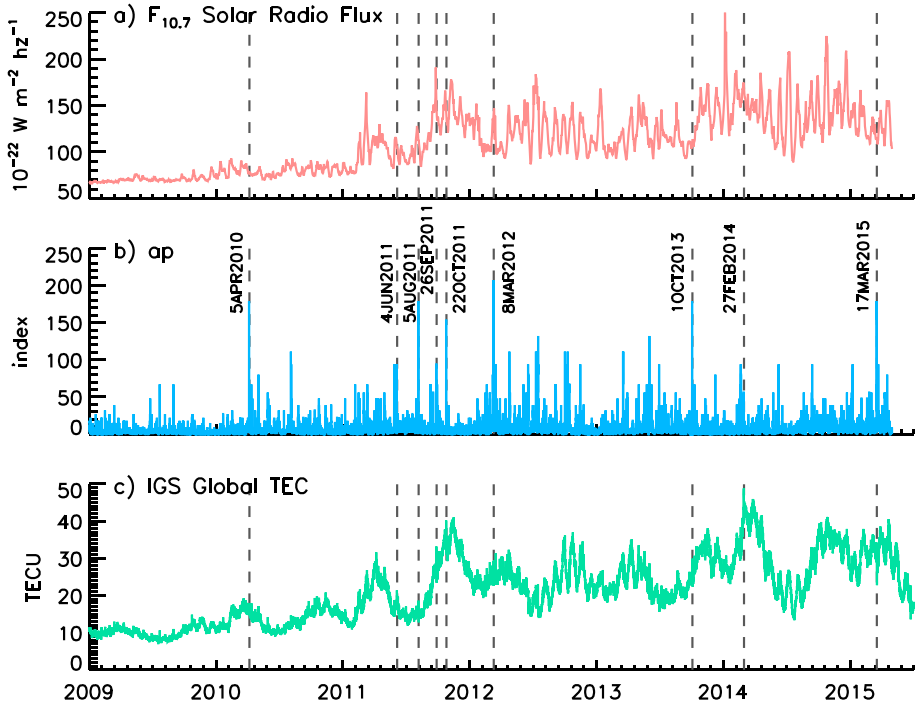

Figure 1. Shown for solar cycle 24 are variations in (a) solar activity indicated by the 10.7 cm radio flux, a proxy for solar EUV irradiance, (b) geomagnetic activity, indicated by the *ap* index, and (c) global TEC determined by integrating 2-hourly IGS TEC maps. The vertical dashed lines indicate the times of nine significant events, for which Table 1 provides more detail.

There is one event (5 August 2011) common to both lists, so our final sample consists of nine events. Table 1 lists distinguishing characteristics for all nine space weather events observed at or near Earth.

2.1. Ionospheric Observations

Ionospheric variability can be quantified using observations of ionospheric total electron content (TEC), which are available both locally and globally. We utilize 2-hourly maps of TEC produced by the International Global Navigation Satellite Systems Service (IGS) Ionosphere Working Group to provide a detailed description of ionospheric behavior in response to each of the nine geomagnetic storms in our sample. The TEC maps are constructed from a global network of ground-based GPS receivers [*Hernández-Pajares et al.*, 2009] as a weighted mean of maps produced at four GPS analysis centers. Weekly comparisons of the slant-path TEC measured by a small set of permanent IGS stations and external self-consistency provide validation.

The time series of global TEC, in units of TECU (1 TECU = 10^{16} electrons m^{-2}), shown in Figure 1 is obtained by integrating the TEC in the IGS maps (resolution 5° × 2.5° longitude × latitude), adjusted for area by cosine (latitude). The degree of the ionosphere's TEC response to the significant geomagnetic events is not readily

Table 1. Properties of Significant Cycle 24 Geomagnetic Storms

						Positive TEC		Negative TEC			
Event	Arrival Time	VB_z (mV/m)	Max(*ap*)	Max(*Kp*)	Min(*Dst*)	Bckd	Max	Bckd	Min	ΔTEC	WAAS Coverage
Apr 2010	4/5/10 09:00	−4.9	179	8− (G4)	−81	15.2	+2.2	15.4	−0.3	2.5	93%
Jun 2011	6/4/11 21:00	−4.2	94	6+ (G2)	−45	17.4	+4.0	18.2	−1.0	5.0	66%
Aug 2011	8/5/11 18:00	−8.8	179	8− (G4)	−115	14.7	+3.9	14.8	−2.0	5.9	45%
Sep 2011	9/26/11 13:00	−12.1	94	6+ (G2)	−118	26.4	+6.8	25.4	−2.0	8.8	41%
Oct 2011	10/24/11 19:00	−6.2	154	7+ (G3)	−147	34.1	+6.1	33.4	−2.6	8.7	0%
Mar 2012	3/9/12 01:00	−8.9	207	8 (G4)	−131	24.8	+4.5	25.6	−3.0	7.5	>99%
Oct 2013	10/2/13 02:00	−11.6	179	8− (G4)	−67	24.3	+5.4	24.3	−1.4	6.8	>99%
Feb 2014	2/27/14 17:00	−4.3	56	5+ (G1)	−94	40.2	+8.3	39.9	−0.5	8.8	47%
Mar 2015	3/17/15 05:00	−9.2	179	8− (G4)	−223	30.0	+3.7	30.7	−7.1	10.8	73%

discernible from the time series of global TEC variability in Figure 1, because TEC varies continuously throughout the solar cycle in response to changes in solar extreme ultraviolet radiation (for which the $F_{10.7}$ index in Figure 1 is a proxy index), with semiannual and annual oscillations whose amplitudes increase with increasing solar activity [*Lean et al*., 2011], and significant diurnal variability. An ionospheric storm event is thus superimposed on a strongly varying background from which its impacts must be extracted.

Effects of individual storms on global TEC emerge clearly when focus is confined to times around the events. Accordingly, Figure 2 shows the temporal evolution of global TEC at the times of each of the nine geomagnetic storms, with the simultaneous evolution of *ap*. Also shown for each of the events is the diurnal cycle at that time, obtained as the average over 11 quiet days ($ap < 30$) centered on the day of the event. The grey shading indicates the 1σ standard deviation of this "local" diurnal cycle and provides a measure against which to assess the ionospheric impacts of each geomagnetic event.

Figure 2 shows that during a solar storm global TEC typically increases above its quiescent value and then decreases below that value. Table 1 therefore lists background levels for both positive and negative phases and indicates the maximum change in global TEC relative to these backgrounds ("TEC Max" and "TEC Min"). The ΔTEC column adds the magnitudes of the positive and negative peak changes to provide an overall measure of ionospheric impact.

In addition to comparing levels of both maximum and minimum storm-related global TEC changes, we also consider another method of quantifying ionospheric impact, albeit one that is local to North America, using the aforementioned WAAS. The WAAS is a network of ground-based reference stations used to monitor GPS satellite signals and provide real-time corrections to GPS positions, thereby improving GPS positional accuracy. It is used in aviation for high precision instrument landing approach procedures within North America. Geomagnetic storms can cause quantifiable degradations in WAAS coverage across the continental United States (CONUS), and records of this are maintained by the Federal Aviation Administration (FAA). The WAAS effects provide a useful measure of ionospheric impact for North America [*Datta-Barua et al*., 2014]. The last row of Table 1 indicates the minimum CONUS WAAS coverage during the storm, with 100% indicating no degradation whatsoever, and 0% indicating complete loss of service within CONUS. Recall that our sample was defined to include the events that produced the five biggest WAAS degradations induced by solar events in cycle 24.

2.2. Solar and Heliospheric Observations

In the STEREO epoch, two heliospheric imagers (HI1 and H12) on each of the two STEREO spacecraft observe the passage of CMEs over Earth, with two coronagraphs (COR1 and COR2) providing observations of the CMEs close to the Sun. To establish in detail the nature of the CMEs responsible for each of the nine geomagnetic storms, we use these observations in combination with observations from a third imager, the Large Angle and Spectrometric Coronagraph (LASCO) [*Brueckner et al*., 1995], on the Solar and Heliospheric Observatory (SOHO). The two STEREO spacecraft have orbits that drifted away from Earth after their 2006 October launch, with STEREO-A operating ahead of the Earth in its orbit around the Sun and STEREO-B trailing behind. SOHO operates near Earth at the L1 Lagrangian point. It is this multiviewpoint STEREO and SOHO imagery, combined with STEREO's ability to track coronal mass ejections (CMEs) in images continuously from the Sun all the way to Earth, that allows for a far more extensive analysis of CME morphology and kinematics than was possible in past solar cycles.

SOHO observes CMEs with the C2 and C3 coronagraph constituents of LASCO. Each STEREO spacecraft carries four white light telescopes that observe at different distances from the Sun, all of which are part of a package of instruments called the Sun-Earth Connection Coronal and Heliospheric Investigation [*Howard et al*., 2008]. Two coronagraphs, COR1 and COR2, observe the solar corona at different distances from the Sun, and two heliospheric imagers, HI1 and HI2, monitor the interplanetary medium in between the Sun and Earth [*Eyles et al*., 2009]. Our analysis considers observations from all 10 of the white light telescopes (LASCO/C2, LASCO/C3, COR1-A, COR2-A, HI1-A, HI2-A, COR1-B, COR2-B, HI1-B, and HI2-B).

For all eight of the nine events for which suitable STEREO observations exist we observe bright fronts in HI2 passing over Earth that we associate with the CME responsible for the geomagnetic storms, although in some cases the fronts end up being blends of multiple CMEs instead of single CMEs. Figure 3 shows LASCO/C2, COR2-A, and COR2-B images of the CMEs that we ultimately deem responsible for the geomagnetic storms.

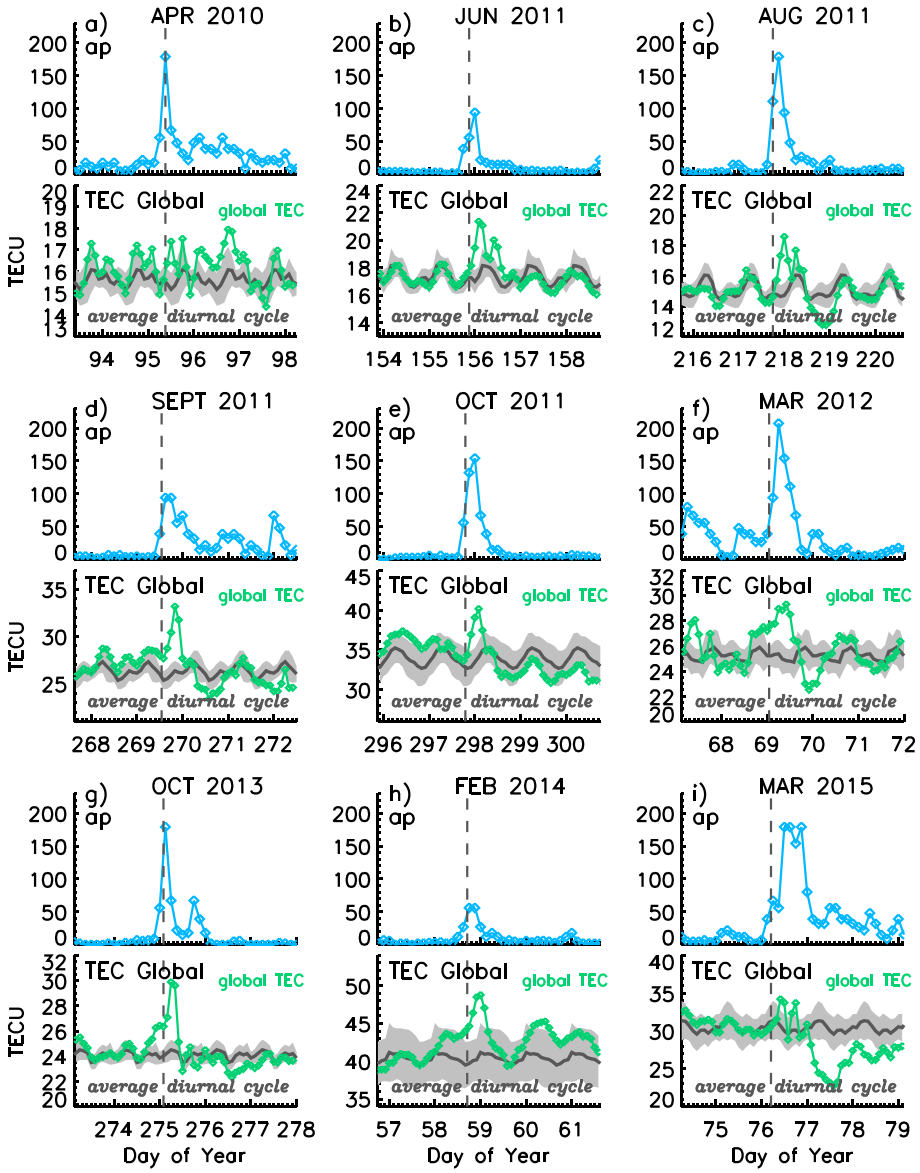

Figure 2. (a–i) Temporal characteristics of nine significant geomagnetic and ionospheric storms in solar cycle 24. For each event, the top panel is the geomagnetic index, *ap*, and the bottom panel is global TEC, with the shaded region indicating the $\pm 1\sigma$ range of the diurnal cycle average for 5 days before and 5 days after (for quiet times with $ap < 30$) the time of arrival of the CME at Earth, indicated by the vertical dashed lines.

For the October 2011 event, we provide in Figure 4 a larger sample of images, including examples from HI1 and HI2. The location of Earth is noted in the HI2-A field of view, emphasizing that STEREO can track CMEs all the way to 1 AU. The images shown are running difference images, with the previous image subtracted from it to enhance the brightness of the CME front. In contrast, the Figure 3 images are shown after subtracting an image from a quiescent period earlier in the day.

Additional observations that we use to characterize the nine geomagnetic events in our study, especially their arrival time at Earth, are density, velocity, and magnetic field measurements from the *Wind* spacecraft operating at the L1 Lagrangian point near Earth [*Lepping et al.*, 1995; *Maksimovic et al.*, 1998]. Figure 5 displays these observations and indicates with vertical lines the ICME arrival times (to the nearest hour) similarly indicated in both Figure 2 and Table 1. Rather than show the absolute magnetic field magnitude, we show in Figure 5 the *z* component of the field, in geocentric solar magnetospheric (GSM) coordinates, as geomagnetic

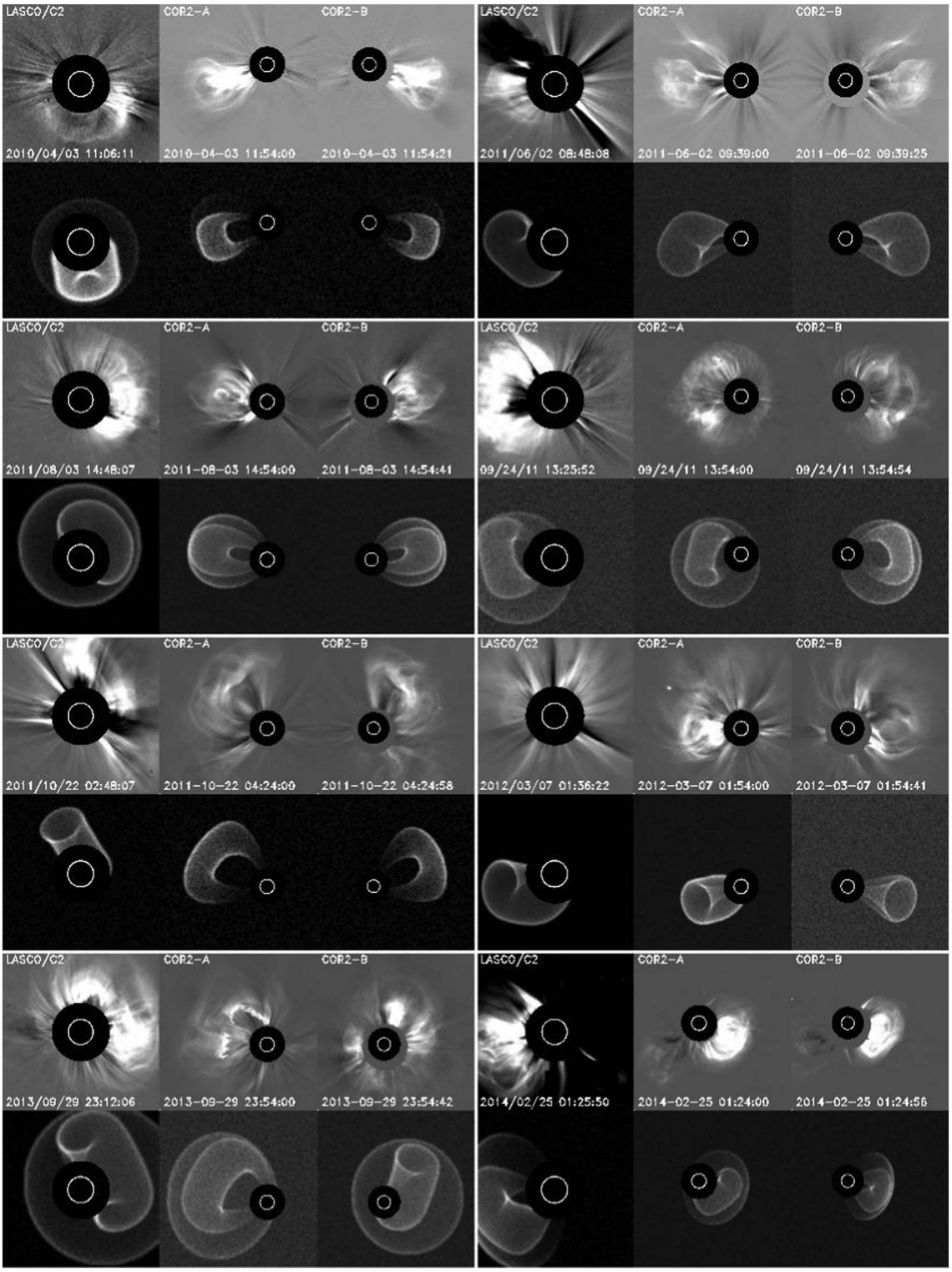

Figure 3. Sample LASCO/C2, COR2-A, and COR2-B images of CMEs responsible for the geomagnetic storms in our sample. Below the images are synthetic images from the 3-D reconstructions of the CMEs, for comparison with the observed images.

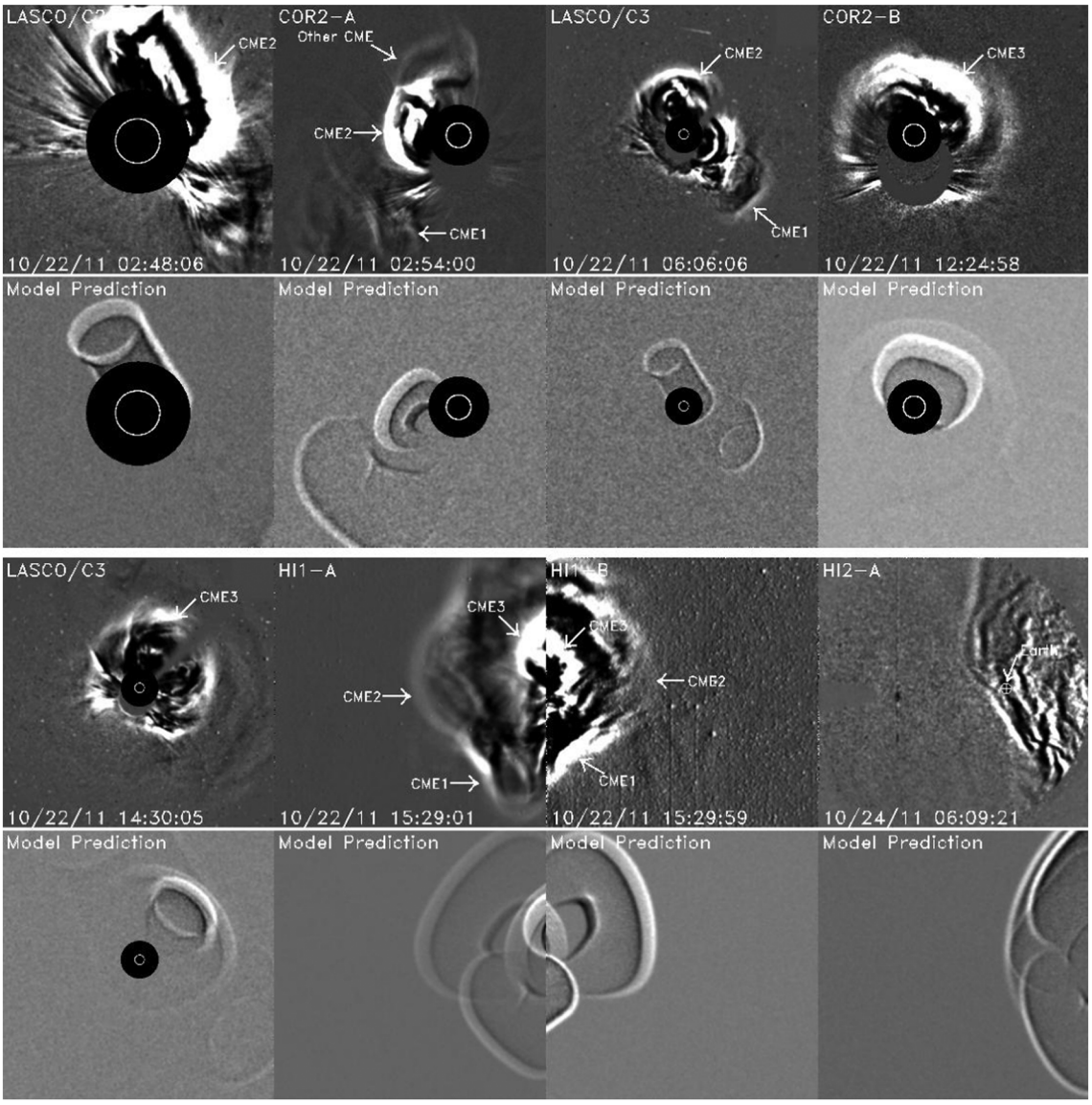

Figure 4. Eight sample images of the 21–22 October 2011 CMEs from the white light imagers on SOHO/LASCO, STEREO-A, and STEREO-B, displayed in chronological order. Below each image is a synthetic image computed from the 3-D reconstruction, for comparison with the observed image above. In the observed images arrows specify the three separate CMEs that are modeled in the time period. It is CME2 that is the geoeffective CME of interest. In the COR2-A image, note the presence of yet another CME marked Other CME that is not modeled.

storms are known to generally be associated with exposure to periods of negative B_z [*Gonzalez et al.*, 1994]. Periods of significant negative B_z are apparent for all nine events but to very different degrees. The March 2012, February 2014, and March 2015 events exhibit lengthy periods of negative B_z, but the other six events see much shorter periods, particularly the April 2010 and October 2013 events, which see significant negative B_z for only a couple of hours at most. The June 2011 event has a different character, with B_z oscillating wildly between negative and positive values.

The second column in Table 1 lists the CME's Earth arrival time, inferred to the nearest hour as described above from Figure 5. Given the known importance of negative B_z for geoeffectiveness, we seek to include in Table 1 a B_z related quantity for each event, although it is not a simple matter to reduce the wide variety of B_z behaviors in Figure 5 to a single quantity. Past work has shown that multiplying the wind velocity times B_z (e.g., VB_z) and computing the mean of this quantity in the relevant time range where B_z is negative lead to a quantity that correlates well with geoeffectiveness [*Wu and Lepping*, 2002; *Wang et al.*, 2003; *Kane*, 2005].

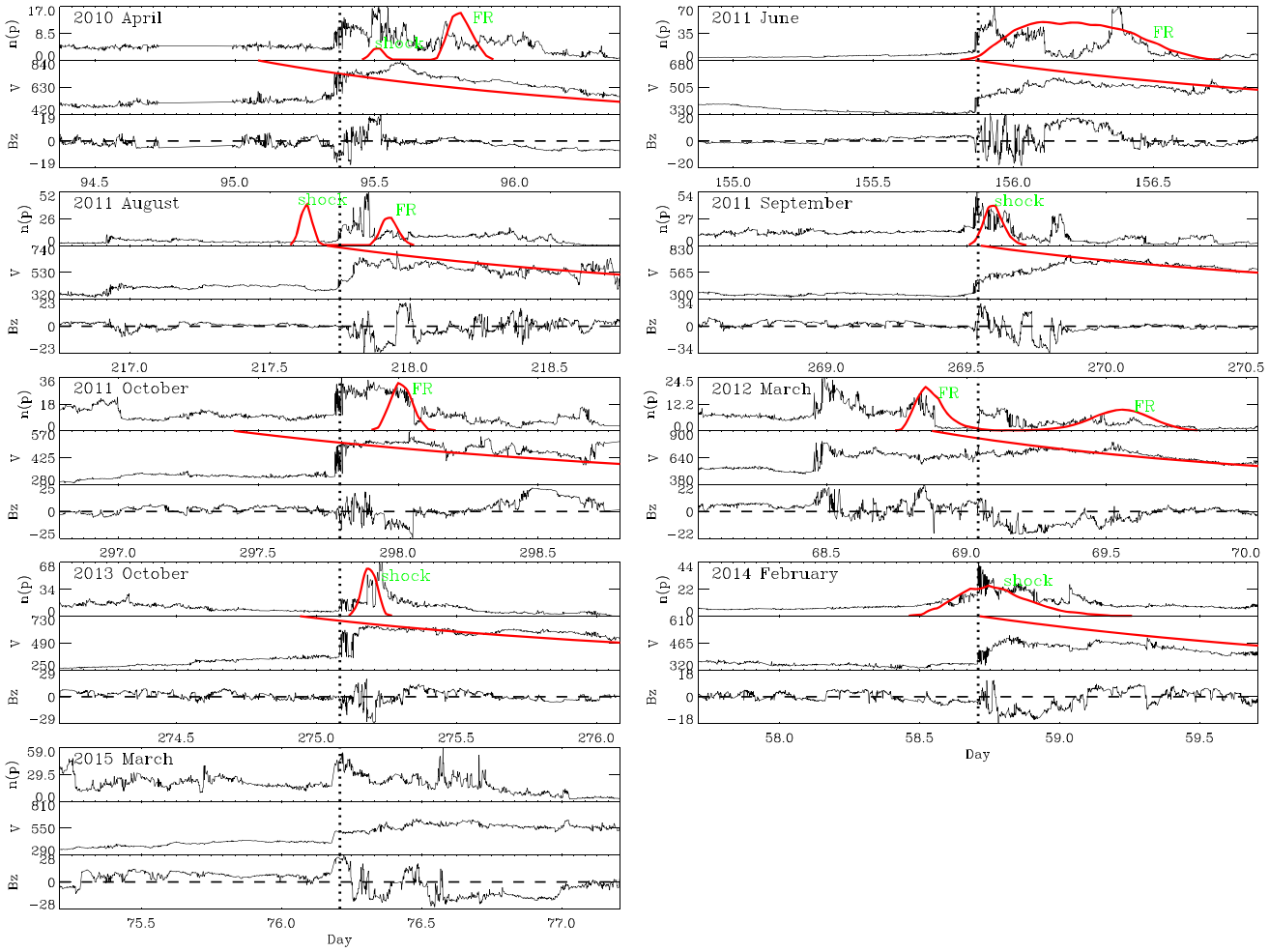

Figure 5. In situ plasma measurements from the Wind spacecraft taken at the time of the nine geoeffective events of interest. Shown for each event are proton density (in cm^{-3}), velocity (in km s^{-1}), and B_Z (in nT), in a GSM coordinate system. Arrival times of the events at Earth are estimated to the nearest hour and indicated with vertical dotted lines mark the arrival time of the event at Earth to the nearest hour. Red solid lines indicate the density and velocity profiles predicted by the 3-D CME reconstructions described in section 4. Labels in the figure indicate whether density peaks are due to the flux rope (FR) or shock components of the reconstruction.

Thus, we list in Table 1 values for VB_z, in units of mV/m, as in *Wang et al*. [2003]. Table 1 also lists the three magnetospheric activity indices: *Dst*, *ap*, and *Kp*. The *Kp* measure is listed with the associated geomagnetic storm level based on the SWPC scale.

3. Ionospheric Impacts

During a solar storm TEC typically first increases above its normal value (the positive storm phase) and then decreases below that value (the negative storm phase) [*Mendillo*, 2006], and the time series of global TEC in Figure 2 show that this is indeed the case of all of our nine events. For the September 2011 event, for example, TEC exhibits a 26% increase, from a background level of 26.4 to 33.2 TECU, about 7 h after the CME arrives at Earth, followed by a decrease from a background level of 25.4 to 23.4 TECU, 25 h after the CME's arrival.

The data in Table 1 suggest that, at least for our sample of nine significant geomagnetic events in solar cycle 24, ionospheric impacts are not necessarily tightly correlated with geomagnetic effectiveness indicated by indices. The five strongest events according to *ap* include both the strongest and weakest of the events according to ΔTEC. Even the geomagnetic diagnostics can be inconsistent with each other. The April 2010 event is the best example of this, with the *ap* and *Dst* diagnostics suggesting very different degrees of magnetospheric disturbance, with *ap* implying a more significant storm.

Table 2. Solar Activity Associated With Significant Cycle 24 Geomagnetic Storms

Event	Component	Source Region	Location	Flare	Start Time	CME Trajectory	φ_{fr}(deg)	V_{peak} (km/s)	V_{term} (km/s)
Apr 2010	…	AR11059	S21W2	B7.4	4/3/10 09:04	S16W3	−80	960	666
Jun 2011	CME1	AR11227	S12E38	C2.6	6/1/11 02:37	S10E25	−15	511	511
	CME2	AR11226	S15E20	C4.1	6/1/11 16:51	S2E25	80	633	633
	CME3[a]	AR11227	S15E24	C3.7	6/2/11 07:22	S5E25	−40	1272	840
Aug 2011	CME1[a]	AR11261	N6W30	M6.0	8/3/11 13:17	N10W10	−60	1358	751
	CME2	AR11261	N8W37	M9.3	8/4/11 03:41	N10W25	−65	2133	766
Sep 2011	…	AR11302	N4E57	M7.1	9/24/11 12:33	N0E41	−75	1739	1017
Oct 2011	CME1	AR11319	N8W80	M1.3	10/21/11 12:53	S25W55	−40	428	428
	CME2[a]	Filament	N25W28	none	10/22/11 01:00	N25E5	−60	720	487
	CME3	AR11314	N25W69	M1.3	10/22/11 10:00	N45W65	30	986	420
Mar 2012	CME1	AR11429	N30E35	X5.4	3/7/12 00:02	N40E40	−65	2896	1464
	CME2[a]	AR11429	N29E30	X1.3	3/7/12 01:05	S15E30	−10	1888	1157
Oct 2013	…	Filament	N4W27	C1.2	9/29/13 21:43	N15W17	−65	1229	627
Feb 2014	…	AR11990	S12E79	X4.9	2/25/14 00:39	S20E67	−40	1508	927
Mar 2015	…	AR12297	S9W26	C9.1	3/15/15 01:15	…		…	…

[a]The component associated with the geomagnetic storm.

We will describe in section 4 our measurements of CME speeds, which are listed in Table 2. The peak velocity (V_{peak}), mean VB_z, *ap*, and *Dst* are explicitly compared in Figure 6 with both TEC_{max} (positive storm phase maximum global TEC increase) and TEC_{min} (negative storm phase maximum global TEC decrease) from Table 1. In Figures 6a–6h a least squares linear fit is made to the data, and a correlation coefficient (*r*) and slope with uncertainty are quoted to indicate the significance of the correlation. Neither TEC_{min} nor TEC_{max} correlates very strongly with velocity or VB_z. The most striking correlation is between *Dst* and TEC in the negative phase (Figure 6h). In contrast, there is only a weak correlation if *ap* is used instead of *Dst* (Figure 6g), so in the negative phase *Dst* seems to be a better indicator of ionospheric response than *ap*. This is a surprising result, considering that *Emmert et al*. [2014] have found that in statistical models of TEC and thermosphere density *ap* and *Kp* are better predictive indices than *Dst*. As for the positive phase, Figure 6d indicates no correlation between TEC_{max} and *Dst*. Surprisingly, Figure 6c seems to imply that TEC_{max} actually goes down as *ap* goes up, which is very counterintuitive. We propose that this is actually an artifact of the negative TEC correlation seen strongly in Figure 6h and weakly in Figure 6g. If the negative phase is more strongly correlated with the *ap* and *Dst* indices, then for particularly strong storms the negative phase can essentially suppress the positive phase, leading to the unexpected anticorrelation in Figure 6c.

Although useful for the purposes of simply comparing ionospheric storms with each other, the global TEC measurements shown in Figures 1 and 2, listed in Table 1 and used in Figure 6, obscure considerable complexity in the ionosphere's response to a solar-induced geomagnetic storm. In reality, there is a large amount of regional variability, which differs distinctively in the positive and negative phases. We compare in Figure 7 characteristic maps from the positive TEC phases of all nine storms in our sample. The maps are constructed by removing an 11 day average diurnal cycle at each grid point, using only those times for which $ap < 30$, and they thus represent the changes in TEC relative to the (regionally dependent) varying, geomagnetically quiet background. All of the cycle 24 ionospheric storms show notable regional and temporal similarities among their initial, positive phases, where about 4 h after the arrival of the CME at Earth, TEC begins to increase at midlatitude to high latitude at those longitudes where the diurnal TEC is near maximum values (i.e., during local day time).

Of the nine ionospheric storms, only the October 2011 event decreased CONUS WAAS coverage all the way to 0% (see Table 1). Figure 2 and Table 1 show that the temporal behavior of global TEC during this particular ionospheric storm exhibited a typical storm response profile, with an initial positive phase in which TEC increased from a background value of 34.1 to 40.2 TECU (~18%) globally followed by a negative phase that commenced about 15 h after the CME's arrival at Earth, reaching a maximum depletion from a background level of 33.4 to 30.8 TECU (~8%) about 45 h after the CME's arrival at Earth.

We choose the September 2011 and March 2015 events as representative events, having particularly strong positive and negative TEC phases, respectively (see Table 1), and show in Figures 8 and 9 sequences of 2-hourly maps of TEC changes associated with these ionospheric storms. The observed TEC increase is

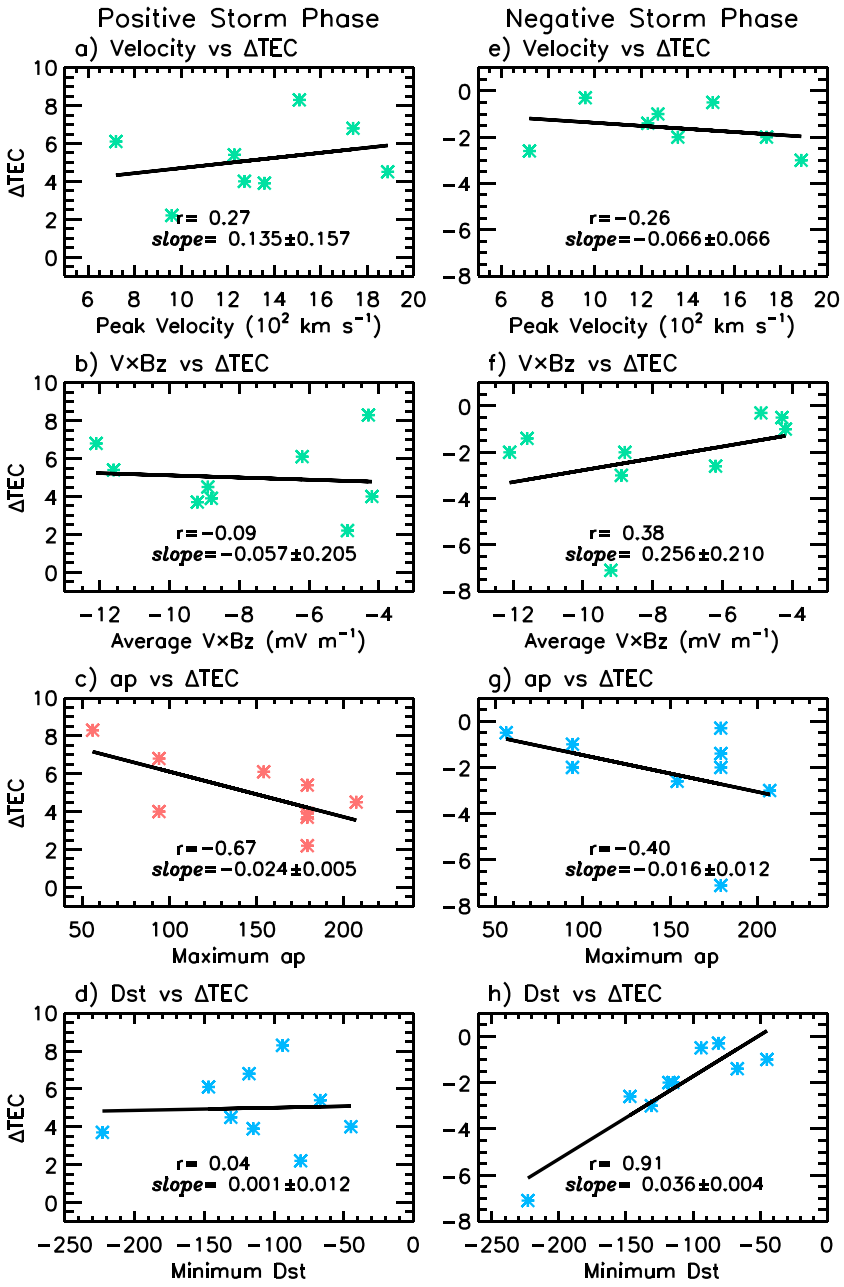

Figure 6. Comparison of peak CME velocity, VB_z, *ap*, and *Dst* indices with global TEC changes, measured for nine ionospheric storms listed in Table 1 during the (a–d) positive ionospheric storm phase and (e–h) negative ionospheric storm phase. The solid lines are linear trends fitted to the data; the slope magnitude and uncertainty are given in each plot. The strongest correlation is of *Dst* with the TEC decrease in the negative storm phase (Figure 6h). The slope of 0.036 ± 0.004 and correlation coefficient indicate that this relationship is highly significant.

largest in the sunlit regions near and just to the east of the local noon line. Possibly, there is some modest depletion near the magnetic equator. The positive phase of an ionosphere storm is likely associated with equatorward neutral winds and large-scale atmospheric gravity waves launched in the auroral zone that travel to the midlatitudes and move *F* region plasma up the field lines to higher altitudes where recombination is slow [e.g., *Balan et al.*, 2010]. Notable in this storm is the plume of enhanced TEC at dusk (0 UT–6 UT) that extends from the Caribbean, across Florida and through the central United States (see Figure 8). This phase of the storm lasts 6 to 8 h, following which the TEC enhancements subside and merge into the negative storm phase.

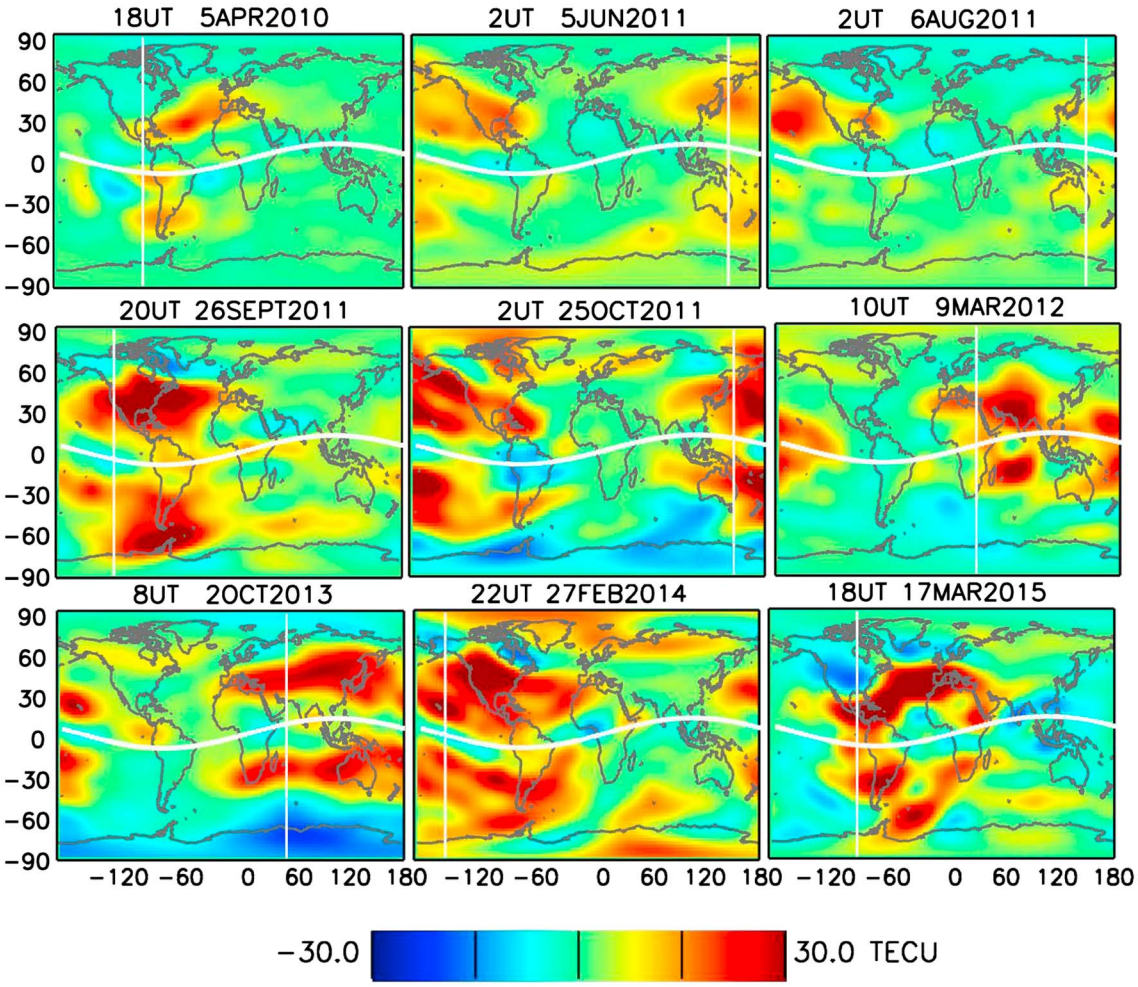

Figure 7. Maps of TEC taken near the maximum of the positive TEC phase of the nine ionospheric storm periods. The vertical lines indicate local noon.

Midlatitude storm enhanced density plumes and the formation of a polar cap tongue of ionization are also associated with the September 2011 event [*Thomas et al.*, 2013]. Regional TEC variations over North America on 26 and 27 September are particularly large. By 18 UT, TEC at midlatitude locations in the vicinity of 60° to 100° W (local noon at 18 UT is at 90°W) increased as much as 30 TECU above the background. There is some modest TEC depletion at low magnetic latitudes. This pattern persists for about 6 h, until about 24 UT.

The impact of the September 2011 ionospheric storm on the WAAS was severe; coverage decreased to 41% over CONUS. Figure 10 (top row) shows in greater detail the TEC just above North America near the peak of the storm (right) and a day before (left). Figure 10 (bottom row) subtracts a 10 day TEC average to make the differences even more apparent. The CME's arrival at 13:00 UT on 26 September 2011 corresponds to early morning over North America. These maps are from the time period 19:30–19:45 UT, midday for the continental United States (near the peak of the local diurnal cycle). It is the large east-west gradients associated with this plume that are responsible for the particularly severe WAAS outage during this storm [*Datta-Barua et al.*, 2014].

The negative ionospheric storm phase is notably weaker than the positive phase for all but one of our events (the March 2015 one) and cannot be readily discerned in Figure 8 for the September 2011 case. It is most evident in Figure 9 (bottom row) for the March 2015 event, for which the percentage negative phase reduction of 23% is more than a factor of 2 larger than for the other eight events in our sample. (The next largest decrease of 12% globally occurred for the March 2012 event.) The March 2015 event produced a dramatic decrease of 7.1 TECU globally, and depletions of as much as 30 TECU in the vicinity of Asia and Australia

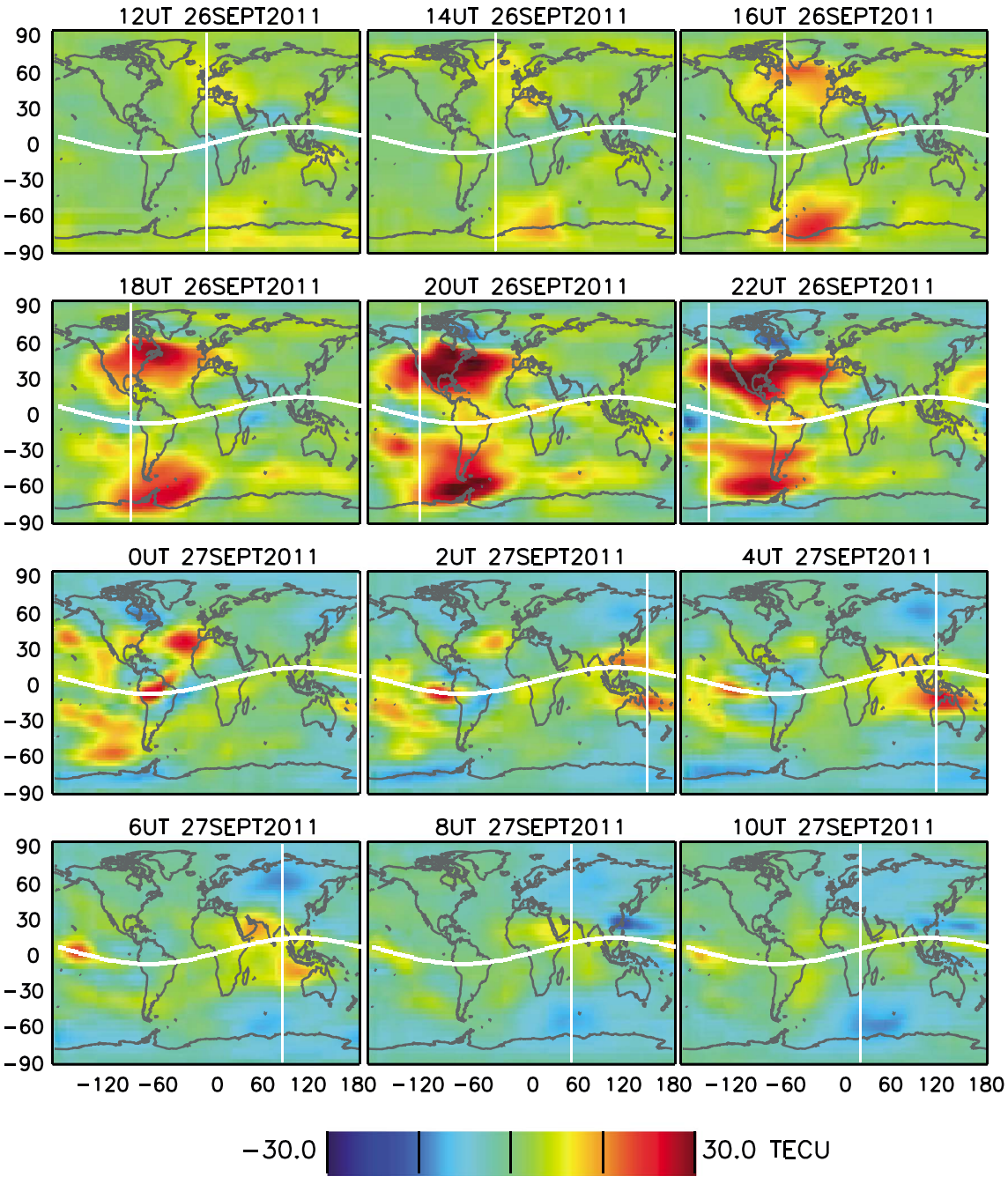

Figure 8. Evolution of 2-hourly TEC during 26 and 27 September 2011, characterizing the ionosphere's regional responses to the 24 September 2011 CME that reached Earth at 13:00 UT on 26 September. The vertical white lines indicate local noon.

beginning around 2 UT on 18 March 2015. The mechanisms supposed for the negative phase of ionospheric storms involve heating of polar regions by solar energetic particles and electrons precipitating from the magnetosphere, producing subsequent alteration of the neutral thermosphere's temperature and composition that transfers dynamically to lower latitudes [*Fuller-Rowell et al.*, 1994]. The bright aurorae evident in both hemispheres on 18 March 2015 signify the presence of such processes. The negative phases are more regionally and temporally diverse in general, but for the March 2015 event the negative TEC regions appear to develop principally near and to the east of the local noon line, as was the case for the positive TEC regions in the positive phase of the storm.

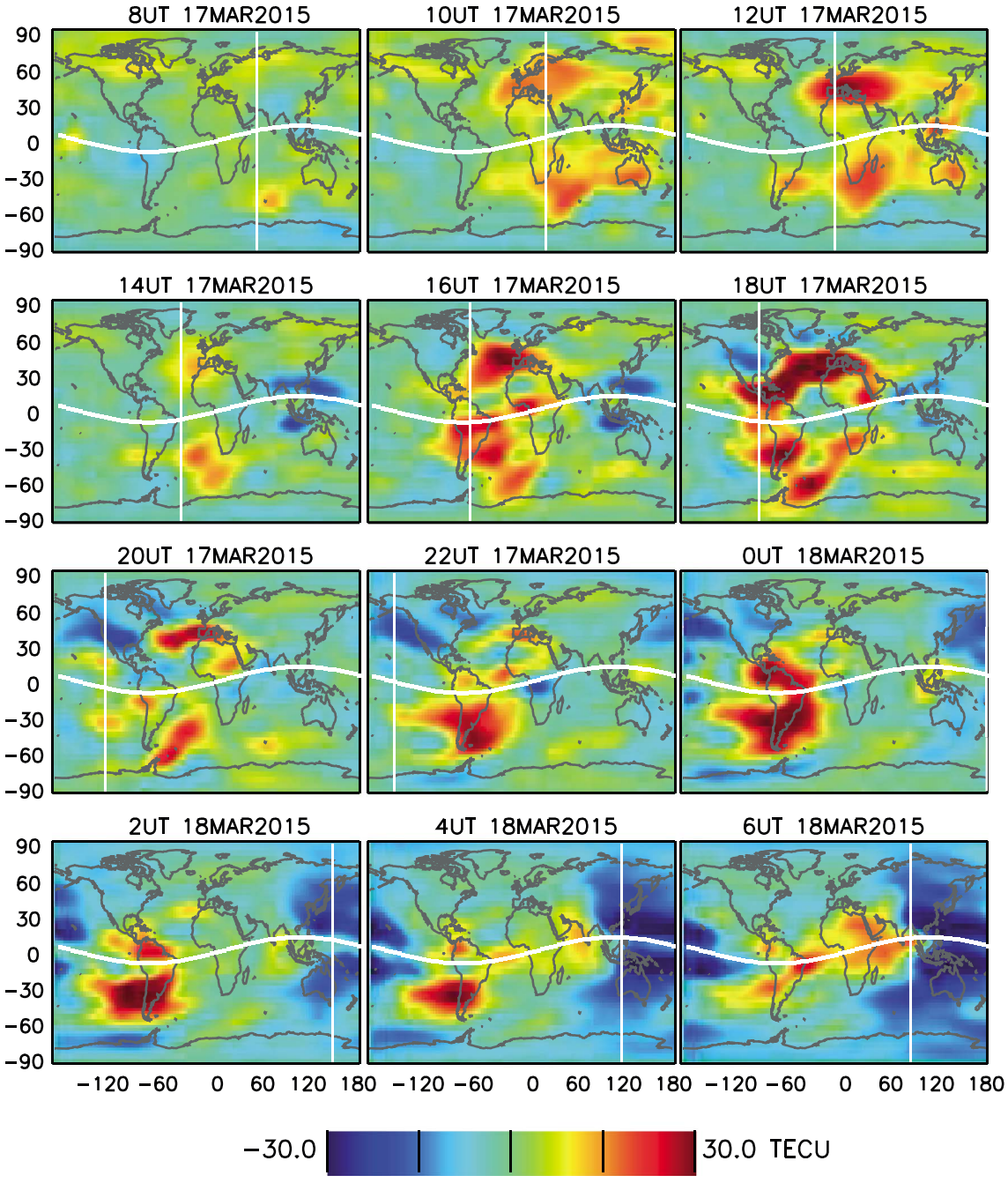

Figure 9. Evolution of 2-hourly TEC during 17 and 18 March 2015, characterizing the ionosphere's regional responses to the 15 March 2015 CME that reached Earth at 5:00 UT on 17 March. The vertical white lines indicate local noon.

The first strong geomagnetic storm of solar cycle 24, on 5 April 2010, exhibits ionospheric behavior that differs starkly from the other events in Table 1. Despite having a large *ap* value of 179, this geomagnetic storm produced only minimal TEC changes. Globally, TEC exceeded 2 TECU for only one 2 h period during the subsequent 2 days after the CME's arrival at Earth. Neither positive nor negative storm phases are readily detected relative to the average diurnal cycle. At 18 UT on 5 April there is a suggestion of modest midlatitude increases in sunlit regions (see Figure 8), which for this storm are located mostly east of CONUS. Since 2010 was a time of low solar activity (Figure 1), overall TEC levels (Table 1) were significantly lower than those observed during most of the other events. Correspondingly, less ionospheric plasma was available for alteration by storm-related compositional and dynamical processes. *Mendillo* [2006] notes that the "modulation in

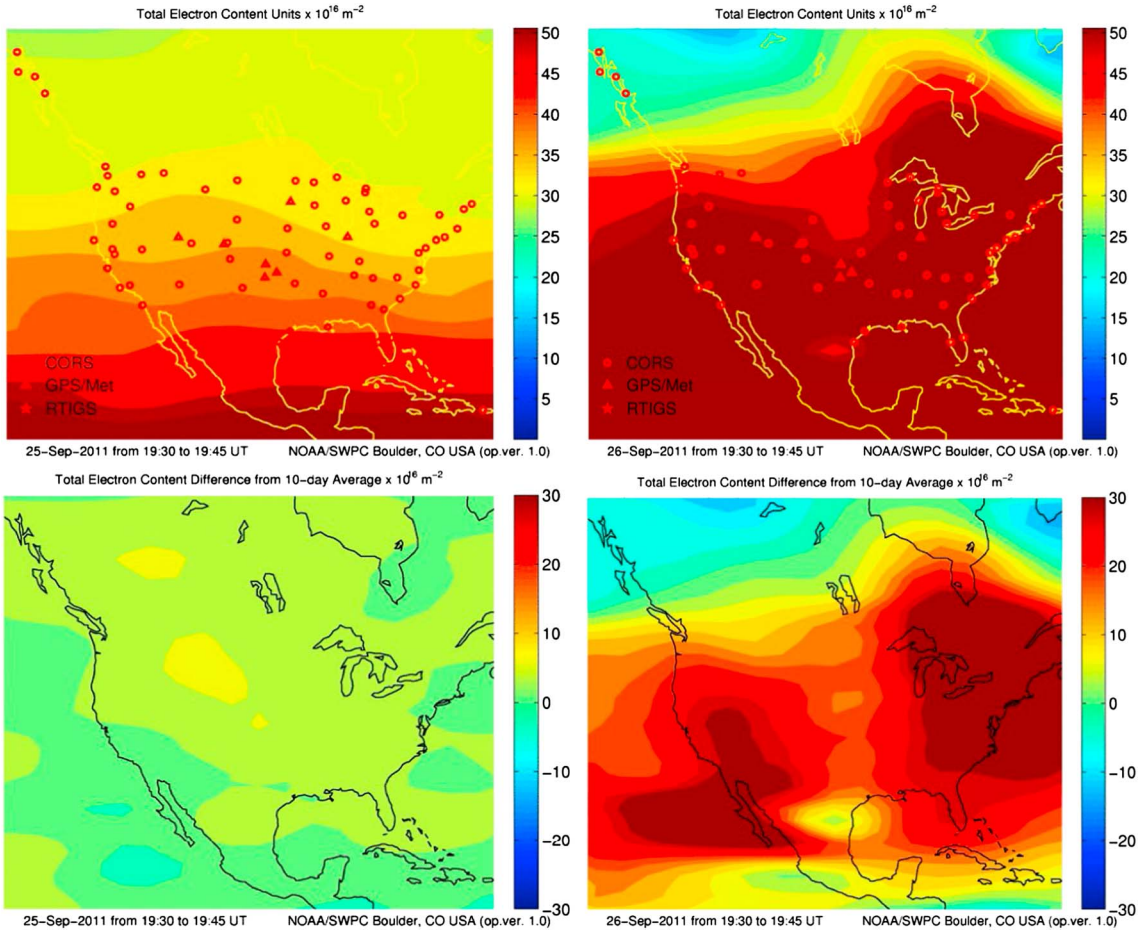

Figure 10. (top row) Measurements of TEC in the ionosphere over North America at two different times. The right panel is during the geomagnetic storm period on 26 September 2011 caused by the 24 September 2011 CME. The left panel shows the TEC map 24 h earlier, for comparison. Red circles, triangles, and stars indicate the locations of various stations used to measure the local TEC. (bottom row) TEC maps for the same times as the upper two panels but subtract a 10 day average to emphasize any enhancements in TEC.

magnitude (of TEC storm effects) depends on ambient conditions." However, significant changes were observed in the thermosphere [*Lu et al.*, 2014]. Note also that while *ap* is high for this event, its $Dst = -81$ value is far less impressive. This event is perhaps an example of *Dst* proving to be a better predictor of ionospheric effectiveness than *ap*, a conclusion supported by Figure 6.

Time of arrival is critical for determining regional impact of an event. Even though each of the ionospheric storms on March 2012, October 2013, and March 2015 impacted the ionosphere sufficiently to alter global TEC relative to the varying background, the USA was largely unaffected by these three events by virtue of the arrival time of each of these CMEs at Earth, with the USA located closer to local midnight rather than local noon during the positive TEC phase. There was no significant WAAS coverage loss for the March 2012 and October 2013 events. For the March 2015 event, the TEC effects grazed the East Coast, and there was a modest WAAS degradation down to 72%. The June 2011 and August 2011 storms did impact WAAS, by virtue of advantageous arrival times, reducing CONUS coverage to 66% and 45%, respectively. The ionospheric effectiveness of these storms are notable in that they occurred during a time of low background TEC, in contrast to the April 2010 event, which proved ionospherically ineffective at such a time.

4. Solar Origins

An effective method for connecting a geomagnetic storm to a specific CME is to examine STEREO's heliospheric images (particularly HI2) at approximately the right time. If such a front is observed, it is then tracked backward into HI1, then to the coronagraph COR2, and finally coronagraph COR1, in order to clearly identify

its solar origin. The preliminary identification of CME candidates is the first step in reconstructing its morphology and analyzing its kinematics, which we describe below. The morphological reconstruction identifies the plasma structure responsible for the geomagnetic storm, and analysis of the CME kinetic motion from the Sun to Earth characterizes its transit speed. Appendix A provides additional considerations for the reconstructions of each of the nine events. For further data/model comparison we provide movies of the events in the supporting information of this article that display the full set of real and synthetic STEREO-A, STEREO-B, and LASCO images.

For four of the events, the geomagnetic storm is easily associated with a single, distinct, bright CME, but for the others (June 2011, August 2011, October 2011, and March 2012) there are multiple CMEs that merge together in the images to varying degrees, requiring analysis of multiple CMEs. The October 2011 event is an example of one of these more complex cases, so the images in Figures 3 and 4 include multiple CMEs.

For eight of the nine events the ICME arrival is clearly marked by density, velocity, and magnetic field peaks near the beginning of the storm events, allowing for a simple identification of the ICME arrival time (see Figure 5). The exception is the March 2012 event, where the geomagnetic storm begins well after the in situ data indicate the arrival of an ICME. The explanation is that two distinct CMEs actually hit the Earth, with the second encounter being the geoeffective one (see section A5).

4.1. Morphological Analysis

Using the observations from three spacecraft, we reconstruct details of the exact morphology, trajectory, and spatial extent of the CMEs. This is possible for all but one of our nine events, the exception being the March 2015 event, for which no STEREO data are available. For the driver of a CME we assume a loop shape, consistent with the understanding that CMEs are fundamentally magnetic flux ropes, i.e., tube-shaped structures permeated with a helical magnetic field, with the two legs of the tube stretching back toward the Sun as the flux rope expands into the interplanetary medium. This physical picture is consistent with measurements of CME internal properties by spacecraft such as Wind [e.g., *Marubashi*, 1986; *Burlaga*, 1988; *Lepping et al*., 1990; *Larson et al*., 1997; *Bothmer and Schwenn*, 1998]. White light images of CMEs are also commonly interpreted as being indicative of a flux rope morphology [e.g., *Chen et al*., 1997; *Gibson and Low*, 1998; *Wu et al*., 2001; *Manchester et al*., 2004; *Thernisien et al*., 2006, 2009; *Krall*, 2007; *Wood and Howard*, 2009]. The flux rope driver acts as a piston, often creating a shock front ahead of it due to its supersonic speed. *Vourlidas et al*. [2012] provide a thorough review of how shock fronts and flux ropes are inferred from white light imaging.

Operating within the flux rope plus shock paradigm, we reconstruct the 3-D morphology of CMEs with the same procedures used in the past to model CMEs with similar appearances. *Wood and Howard* [2009] and *Wood et al*. [2011, 2012] provide detailed information about our approach. In summary, the approach is to compute synthetic SOHO/LASCO and STEREO images from 3-D density cubes constructed assuming the flux rope plus shock morphology. The 3-D flux rope and shock front components are both parameterized shapes, where we can change the structures in the density cube simply by adjusting the parameters. For the shock front the important parameters are latitude and longitude of trajectory, width (σ), and a single parameter (α) affecting the flatness of the front. For the flux rope there is a separate latitude and longitude of trajectory, there are σ and α parameters for both the inner and outer edges of the rope, and size scales relative to the shock front for both the inner and outer edges. Finally, there is a rotation angle for the flux rope relative to the ecliptic plane (φ_{fr}) and an ellipticity for the flux rope channel (η_{fr}) [*Wood et al*., 2011]. The φ_{fr} parameter defines the orientation of the flux rope, specifically the rotation angle of the west leg of the flux rope relative to the ecliptic, with $\varphi_{fr} = 0°$ corresponding to a flux rope oriented parallel to ecliptic plane, and $\varphi_{fr} = 90°$ corresponding to a flux rope oriented perpendicular to the ecliptic. This totals 14 morphological parameters, excluding a few nonmorphological parameters describing how mass is actually distributed on the shock front and flux rope surfaces.

We iterate different parameters to obtain a density cube that best reproduces the observed images. Below the three images in Figures 3 and 4 are synthetic images computed from this model, with some random noise added to the synthetic images for esthetic reasons. The model reproduces the CME's appearance in the real images reasonably well. More extensive comparisons between real and synthetic images are presented in the movies available in the supporting information of this article. Figure 11 shows the final best fit models for eight events, and Figure 12 shows slices through the models in the ecliptic plane, so as to illustrate the

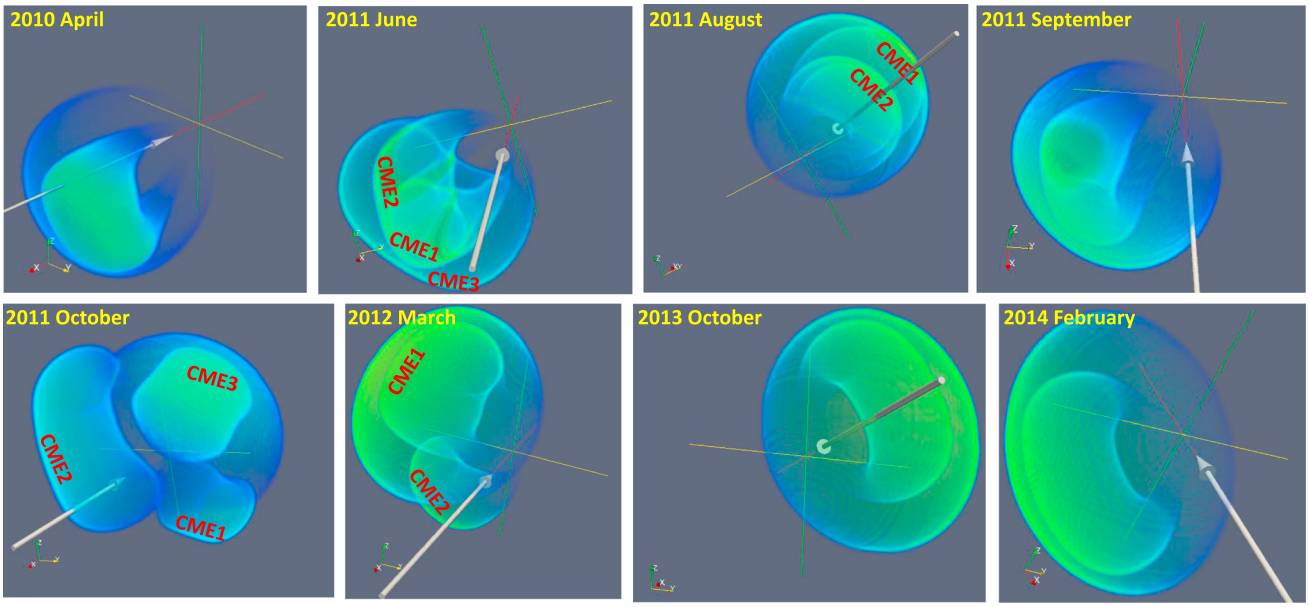

Figure 11. Three-dimensional reconstructions of CMEs responsible for geomagnetic storms, with multiple CME candidates being studied in some cases. Each CME is modeled as a flux rope driver, often with a lobular shock ahead of it in cases where images clearly show a distinct, visible shock in front of the CME ejecta. For cases with multiple CMEs, labels are provided for the individual flux rope components, and in these cases the relative positions of the individual CMEs are shown as they would be as the leading CME approaches 1 AU. In each panel, the *xy* axis is the ecliptic plane, with the *z* axis pointing toward the north ecliptic pole, and the arrow indicates Earth's trajectory through the structure as it expands outward.

trajectory and spatial extent of the CMEs in this plane. The CME trajectory directions derived in this fashion are considered reliable to within about 5°. Table 2 lists the CME trajectories inferred from all of our CME reconstructions.

The September 2011 event is an interesting example of how not only can a CME shock by itself be geoeffective, but it can be geoeffective far from the center of the CME. The in situ data in Figure 5 indicate the presence of a shock, followed by a disturbed region, which persists for a long time after the shock passage. There is no evidence for a flux rope behind the shock, which would be defined by a region of strong, organized, rotating magnetic field behind the shock. This is consistent with our morphological reconstruction, which suggests that while the CME shock hits Earth, the flux rope passes well to the east (see Figures 11 and 12). Even the shock barely grazes Earth.

4.2. Kinematic Analysis

Measurements of CME kinematics from STEREO data begin with measurements of the elongation angle of the CME leading edge from the Sun, ϵ, as a function of time. For example, for the 24 September 2011 CME that we identify as the source of the 26 September 2011 geomagnetic storm, STEREO-B provides the best vantage point for tracking the CME from the Sun to 1 AU. (The STEREO movie of the September 2011 CME available in the supporting information most clearly shows the CME front being tracked from the Sun to 1 AU.) The elongation angles measured from STEREO-B images are converted to actual distances from Sun center, *r*, which requires assumptions about CME front geometry. We use the so-called "Harmonic Mean" assumption from *Lugaz et al.* [2009], which assumes CMEs can be approximated as spheres centered halfway between the Sun and the leading edge. This leads to

$$r = \frac{2d \sin\epsilon}{1 + \sin(\epsilon + \varphi)}$$

where *d* is the distance of the observer (STEREO-B in this case) from the Sun, and φ is the angle between the observer and trajectory of the center of the CME. The trajectory angle φ is determined from the morphological part of the analysis described above, which yields $\varphi = 55.6°$. Figure 13 (top) shows the resulting distance measurements for the September 2011 event. Assuming that the CME structure expands self-similarly, the kinematic model provides crucial information on how the scale size of the density cube changes with time.

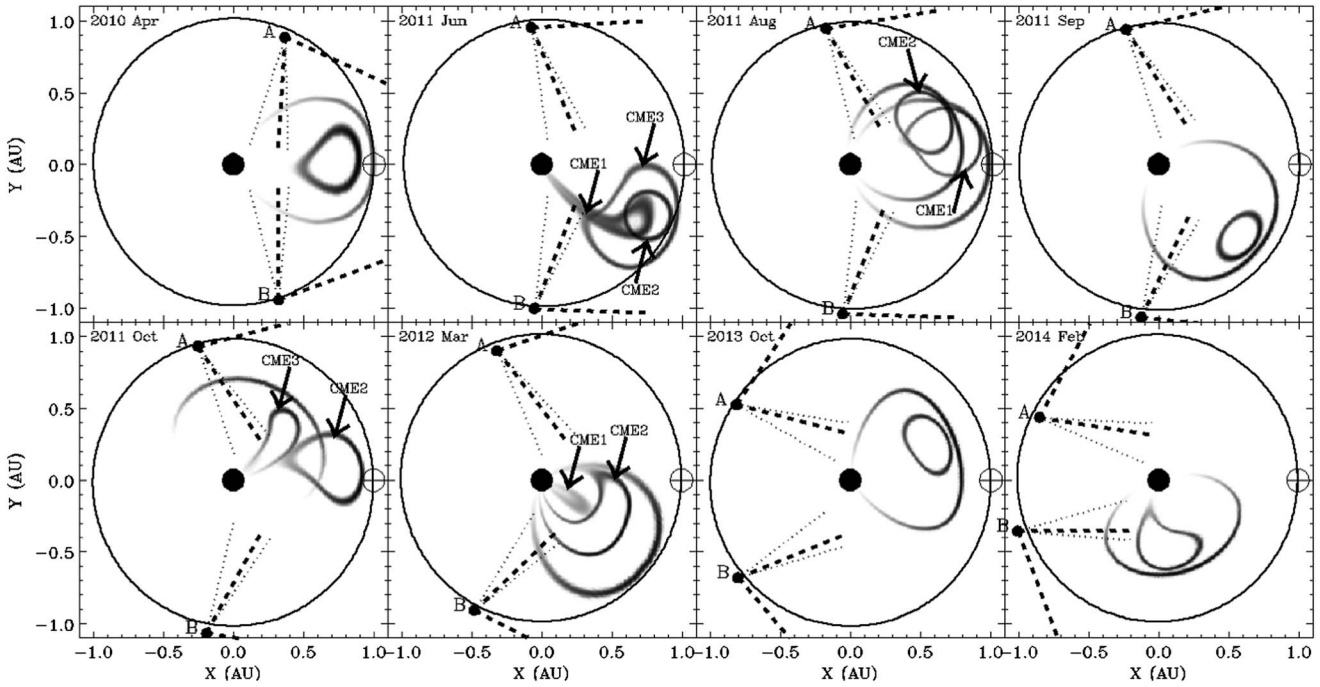

Figure 12. Ecliptic plane maps comparing the orientation and morphology of eight of our nine geomagnetic storms, in heliocentric Earth ecliptic coordinates, showing the positions of STEREO-A, STEREO-B, and Earth. Note that SOHO observed the Sun from near Earth at the L1 Lagrangian point. The spatial extent of each CME (or CMEs) in the ecliptic plane is indicated using a slice through the 3-D reconstructions. Dotted and dashed lines indicate the fields of view of the HI1 and HI2 heliospheric imagers on board the STEREO spacecraft.

There is in practice some iteration between the kinematic and morphological parts of the analysis, as the kinematic analysis requires φ from the morphological analysis, and the morphological analysis requires the kinematic model from the kinematic analysis to know how to expand the density cube.

Continuous velocity and acceleration profiles for the CME are then inferred from the distance measurements using a simple kinematic model. For many fast CMEs in the past, we have used a simple three-phase kinematic model, with a short phase of constant acceleration followed by a phase of constant deceleration as the CME slows, and finally a phase of constant velocity [*Wood and Howard*, 2009; *Wood et al*., 2011, 2012]. We model the 24 September 2011 CME similarly, but this CME seems to be fully accelerated by the time it first appears in COR1-B images, so the first phase is omitted. As in past analyses, we assume 1% uncertainties for the distances measured from COR1 and COR2, 2% uncertainties for HI1 distances, and 3% uncertainties for HI2. These uncertainties have been found in the past to lead to χ^2 values of order 1, as expected if the assumed uncertainties are reasonable. The resulting two-phase fit is illustrated in Figure 13 for the September 2011 event. In this case, the CME initially has a maximum velocity of 1739 km s^{-1} but decelerates at -52.6 m s^{-2} up to 28.9 $R_\odot$, at which point it reaches its final terminal velocity of 1017 km s^{-1}. The 1739 km s^{-1} speed inferred for the driver is easily fast enough that a shock would be expected to exist in front of the CME, consistent with this interpretation of the observed faint leading front. These peak and terminal velocities are listed in Table 2, for this event and the others in our sample, and Figure 14 explicitly shows the CME velocity versus height curve for all of the geoeffective CMEs in the sample.

We note that for our kinematic models, we seek the leading edge of the CME ejecta, as opposed to the shock, so the kinematics in Figures 13 and 14 are for the leading edge of the driver, not the shock. The CME ejecta are generally easier to follow continuously from the Sun to 1 AU. However, the difference in kinematics between the shock and driver is not large, as the driver and shock leading edges are always seen rather close together, and can actually become difficult to distinguish, in HI1 and HI2 particularly.

Finally, we also consider in situ observations in Figure 5 from the Wind spacecraft at L1. Specifically, we ensure that our 3-D model reproduces the CME arrival time at Earth with reasonable accuracy. The red lines in Figure 5 explicitly show the density and velocity time profiles predicted by the 3-D empirical reconstructions.

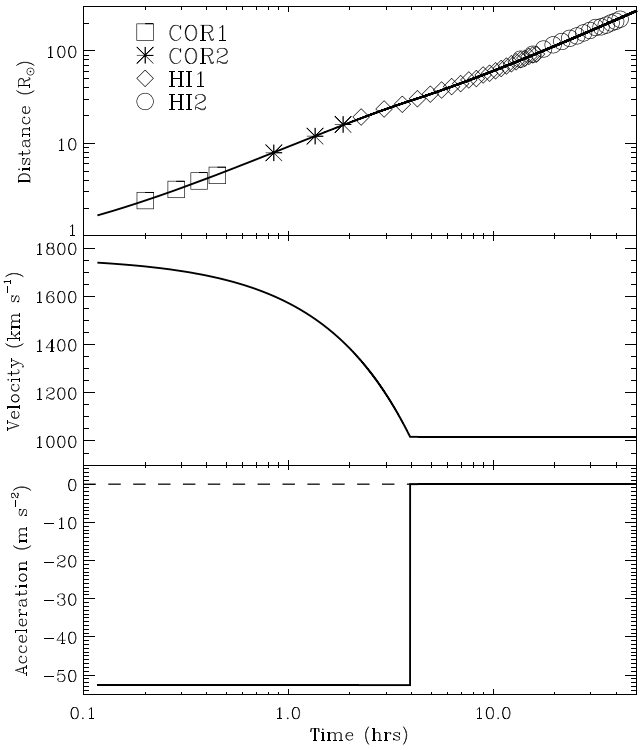

Figure 13. Kinematic model of the 24 September 2011 CME based on measurements from the four white light imagers on board STEREO-B (COR1-B, COR2-B, HI1-B, and HI2-B). The model follows the leading edge of the flux rope component of the CME. It is a simple two-phase model assuming a phase of constant deceleration followed by a phase of constant velocity, yielding the distance, velocity, and acceleration profiles shown in the three panels.

As required, the density peaks are close to the observed Earth arrival time. The velocity profiles show a decrease with time in a manner consistent with the self-similar expansion that is assumed for the events in the 3-D reconstruction. It should be emphasized that with regards to the shock, the model velocity corresponds to the shock propagation speed rather than the speed of material moving through the shock, which is what the in situ data measure. Thus, an exact velocity match is not to be expected.

In practice, projection effects complicate inferences of Earth arrival time from HI2 images of CME fronts passing over the apparent position of Earth, but HI2 data nevertheless provide a valuable tool to identify candidate CMEs [*Möstl and Davies*, 2013; *Shen et al.*, 2014]. The use of STEREO's heliospheric imagers is an improvement over the pre-STEREO situation when no data existed to bridge the gap between LASCO observations of a solar eruption near the Sun and a geomagnetic storm observed days later at Earth.

4.3. Solar Source Region Identification

For all events in our sample, surface activity associated with CMEs of interest are easily identified by looking at X-ray and EUV observations of the Sun at the time when the CME first enters the COR1 or LASCO/C2 field of view. Of particular utility are EUV images from the Atmospheric Imaging Assembly (AIA) instrument on board the Solar Dynamics Observatory (SDO) [*Lemen et al.*, 2012]. Figure 15 locates the solar source regions of the CMEs responsible for the events in our sample, as seen from the vicinity of Earth. The figure uses EUV images (at 19.3 nm) primarily from SDO/Atmospheric Imaging Assembly, but images from the Extreme ultraviolet Imaging Telescope (EIT) on SOHO [*Delaboudiniere et al.*, 1995] are used instead for the April 2010 event, which occurred just prior to the beginning of operations on SDO. Boxes indicate where the surface activity is observed that is associated with the CMEs. Flares are associated with most of our CMEs, and Table 2 lists the X-ray flare strengths, active region (AR) number, and start time, using information obtained from NOAA's Space Weather Prediction Center website. Two of the events (24 October 2011 and 2 October 2013) were not associated with an active region but

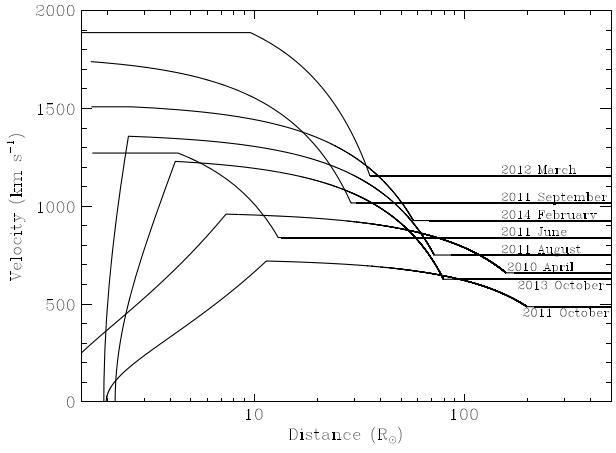

Figure 14. Kinematic models of the CMEs identified as being responsible for the geomagnetic storms in our sample of events.

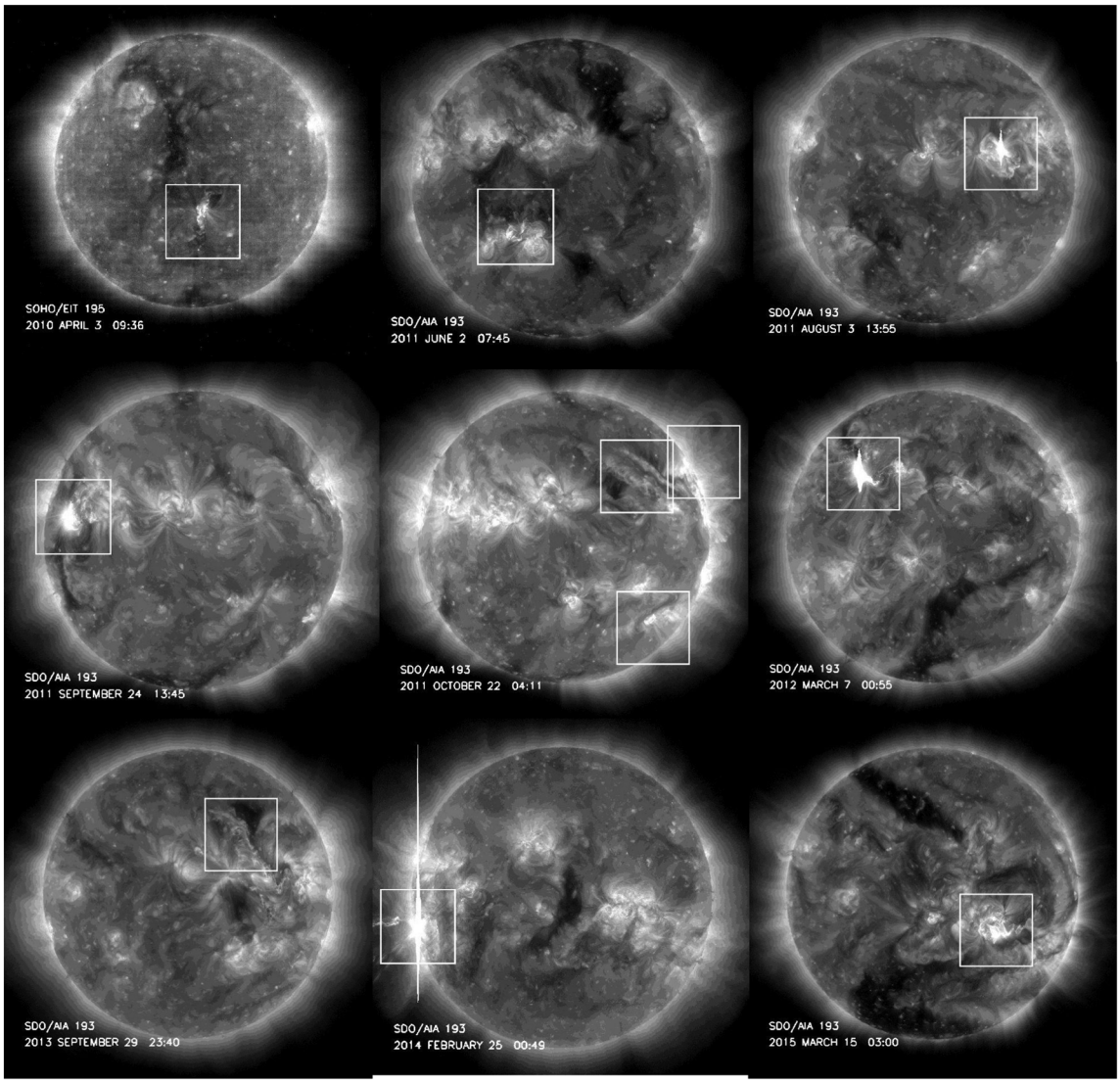

Figure 15. Distribution of EUV emission at 19.3 nm on the Sun's surface, recorded by SDO or SOHO/EIT, at the times of launch of CMEs that produced the six significant geomagnetic and ionospheric storm events shown in Figure 2. Boxes surround the source regions of the CMEs. For the June 2011, August 2011, and March 2012 periods, multiple events are analyzed (see Table 2), but all emanate from the same general area within the displayed box. For the October 2011 event there are three CMEs that are analyzed from three distinct source regions (see Table 2), which are identified with three different boxes, with CME1 coming from the southern region, the geoeffective CME2 from the upper left region, and CME3 from the upper right region.

instead with activity along lengthy filament channels, as noted in Table 2. Surface locations relative to the Sun-Earth line (in ecliptic coordinates) are measured from EUV images and listed in the fourth column of Table 2, for comparison with the CME trajectories listed in the table.

For the example of September 2011, the event began on the Sun at 12:33 UT on 24 September with an M7.1 flare from active region AR11302. The source active region was at a location of N4E57 relative to the Sun-Earth line. The source region and CME trajectory are therefore both well east of the Sun-Earth line, though the CME is directed 16° closer to Earth in longitude than if the CME had expanded radially from the source region. It is interesting to note from Figure 3 that this 16° difference is large enough that if the CME had actually been directed radially from its source region it would have missed Earth entirely.

5. Discussion

Our sample of nine solar storms and associated CMEs in cycle 24 was chosen on the basis of ionospheric impacts and geoeffectiveness. Should such events exhibit some features in common, their characterizations

would enhance space weather forecasting skill. However, our event list is impressively diverse. There are events that altered ionospheric TEC significantly, and events that did not. There are events associated with significant reductions in WAAS coverage, and events for which WAAS was unaffected. There are events associated with strong solar flares (e.g., March 2012 and February 2014) and events associated with little or no flare activity at all (e.g., October 2011 and October 2013). There are events where Earth is hit within 20° of the CME's central trajectory (e.g., April 2010 and August 2011), but there are a surprising number where the central trajectory is far from the Sun-Earth line. In two cases (September 2011 and February 2014) it is over 40° away. Had the September 2011 CME actually been directed radially from its source region it would have missed Earth entirely; the 16° difference of the actual direction from radial (Figure 3) was large enough to redirect it more toward the Earth. Periods of negative B_z are understood to be crucial for geoeffectiveness, and we do find a modest correlation between the average VB_z after the CME's arrival at Earth with the subsequent TEC depletion in the negative storm phase (see Figure 6f). Given the variety of B_z behaviors apparent in Figure 5, it is unclear if it would be possible to forecast ionospheric impacts in all cases even if it were possible to observe B_z significantly prior to Earth impact.

5.1. Ionospheric Impacts

It is potentially helpful for forecasting purposes that the early phases of ionospheric storms are similar with regards to the duration of the positive TEC phase and smooth transition to the negative phase (see Figure 7). This apparent uniformity of the ionosphere's response and the significant correlation of the magnitude of the negative TEC phase globally with *Dst* (Figure 6h) suggest that further statistical characterization of a larger population of ionospheric storms (in cycles 23 and 24) may lead to improved forecasting of the regional morphology and evolution of ionospheric TEC changes up to 12 h after a CME's arrival at Earth. *Immel and Mannucci* [2013] used Jet Propulsion Laboratory TEC maps from 1999 to 2005 to study a UT (or longitude) effect on TEC due to geomagnetic storms. They reported that the Western Hemisphere experiences the largest increases in TEC, especially at southern midlatitudes, and they suggest that the UT effect may be attributed to special characteristics of this region, including the South Atlantic Anomaly and the large change in magnetic declination. Modeling studies have also shown a longitude effect on enhanced TEC related to high-latitude electric fields and thermospheric winds [*Sojka et al*., 2012]. As well, the global regional perspective that analyses of the IGS TEC maps afford provides a broad context for interpreting observation at individual sites, such as reported, for example, for storms in equatorial Africa [*Akala et al*., 2013]. The negative phases of the ionospheric storms in solar cycle 24 exhibit TEC decreases peaking about a day after the arrival of the CME at Earth (see Figure 2), but the negative phases are far more regionally and temporally diverse. The very strong correlation (more than 99% significant) that we find between the global TEC negative depletion and *Dst* (Figure 6h) promises a measure of forecast skill. Characterization and forecasting of the negative ionospheric storm impacts are a focus of ongoing work.

The time of arrival of a CME at the Earth plays a major role in determining where the ionospheric impacts occur regionally. The five events in our sample selected on the basis of degrading WAAS the most during cycle 24 all arrived between 13:00 UT and 21:00 UT, with the other four events all arriving outside this time period (see Table 1). This WAAS-effective time range corresponds to an arrival at Earth during CONUS daytime. The bulk of the ionospheric plasma, which is produced by solar EUV radiation, resides over sunlit regions near the magnetic equator. The most WAAS-effective event, the October 2011 ionospheric storm, peaked at dusk and was due to the evening plume that developed. In the particularly lengthy March 2015 ionospheric storm (see Figure 2), a strong poleward surge in the thermospheric wind [*Zhang et al*., 2015] caused a depletion in TEC over North America that possibly reduced its impact on WAAS. It should be emphasized that the events that did not arrive at times advantageous for affecting WAAS may have affected analogous systems in other places, the European Geostationary Navigation Overlay Service, for example. Since the exact time of Earth arrival is crucial for forecasting ionospheric regional variations in response to solar storms, precisely estimating the arrival time at Earth is crucial. Unfortunately, the skill in such forecasting is not high: the 15 h discrepancy in the forecast versus actual arrival time of the March 2015 CME at Earth attests to this. In 15 h the region of high solar EUV produced TEC rotates 225°, considerably shifting the regional location of the storm's primary impacts.

The most recent event in our sample, the March 2015 event, has received much attention recently [*Kataoka et al*., 2015]. Like the September 2011 event, the March 2015 event imparted only a glancing impact to Earth, but global TEC nevertheless increased 3.7 TECU during the positive ionospheric storm phase, followed by the most prominent negative storm phase yet witnessed in cycle 24, a global TEC decrease of 7.1 TECU. The

dramatic aurora, visible in both the Northern and Southern Hemispheres, concurrent with this decrease attests to a prominent role of precipitating electrons in polar regions as its cause. Space weather agencies initially forecast a modest G1 event, not the subsequent G4 event, and predicted the arrival time at Earth to be 15 h later than it actually was.

5.2. Solar Origins

Geoeffective CMEs clearly tend to be massive, both close and far from the Sun. Only massive and bright CMEs can be tracked all the way into and through the HI2 field of view, so it is noteworthy that all the geoeffective CMEs in our sample were easily trackable from the Sun to 1 AU, without exception. Another clear geoeffective CME characteristic is a fast velocity. All the events are accelerated to relatively high speeds close to the Sun and are then decelerated in the interplanetary medium between the Sun and Earth. Not one of our geoeffective events is associated with a slow CME that merely accelerates up to the ambient solar wind speed close to the Sun. Slow events dominated event lists in the solar minimum period of 2009–2010 [e.g., *Kilpua et al*., 2014], but they are also common in more active periods (e.g., the "CME1" components of the June 2011 and October 2011 events in Table 2). However, Figure 14 shows that although all our events are relatively fast there is still an impressive range of peak velocities, from the very modest 720 km s^{-1} speed of the October 2011 CME to the very fast 1888 km s^{-1} velocity for the March 2012 event. Despite the clear tendency for geoeffective CMEs to be fast, the correlation of velocity with TEC changes listed in Table 2 and shown in Figure 6 is not significant.

The CME with among the largest ionospheric impact, on October 2011, was also the slowest, its peak speed of 720 km s^{-1} is unremarkable (see Table 2). According to our reconstruction of this event, Earth encounters the southern end of the northeast-southwest oriented flux rope of CME2, with a central trajectory at N25E5 relative to Earth. It is noteworthy that this geoeffective CME begins with no clear flare at all. There is a dramatic restructuring of the magnetic field around a lengthy filament channel beginning at about 1:00 UT, apparent in Figure 15. The filament channel activity morphologically resembles a very large two-ribbon flare but without the dramatic overall brightening that would identify it clearly as a flare in the disk-integrated X-ray light curve.

Some past studies of the March 2012 event have missed or ignored the actual CME that we identity as geoeffective. Our reconstruction of this event suggests that Earth encounters the west leg of the CME2 flux rope (see section A5), and the two density peaks predicted by the model (see Figure 5) indicate when Earth enters and then exits the flux rope. The first peak is about 4 h earlier than the arrival time marked in the figure. In contrast, some prior studies have simply associated the geomagnetic storm with the brighter and faster CME1 [*Davies et al*., 2013; *Liu et al*., 2013; *Rollett et al*., 2014]. Our assessment agrees with *Möstl et al*. [2014] and *Patsourakos et al*. [2016] who also previously identified CME2 as the true Earth-directed event, with the caveat that the shock that initially hits Earth midday on 8 March is actually associated with CME1 in our reconstruction, even though it is CME2's arrival that later produces the geoeffective part of the ICME. *Patsourakos et al*. [2016] provide a flux rope reconstruction of both CMEs using the *Thernisien et al*. [2009] approach. Their reconstructed flux rope structures agree reasonably well with our model. Specifically, they find central trajectories of N31E37 and S13E40 for CME1 and CME2, respectively, which can be compared with our N40E40 and S15E30 measurements (see Table 2). With regards to flux rope orientation, *Patsourakos et al*. [2016] find φ_{fr} values of −78° and −33° for CME1 and CME2, respectively, compared to our −65° and −10° measurements (see Table 2). Although slower than CME1, CME2 is ultimately the fastest of the geoeffective CMEs in our sample, as shown explicitly in Figure 14. It is interesting that while the distinct flares associated with CME1 and CME2 are separated by only about 5° on the solar surface, the trajectories of the two CMEs end up 56° apart. The presence of CME1 likely deflected CME2 well south of where it otherwise would have been directed.

Of the parameters used to define the flux rope shapes used in our CME reconstructions, we deem most of insufficient interest to list in Table 2, but we do list the φ_{fr} parameter in the table. This is because one surprising characteristic of our reconstructed CMEs is that the flux ropes seem to have a strong tendency to possess negative values for φ_{fr}. A negative φ_{fr} value basically corresponds to a flux rope with a northeast-southwest orientation. Twelve of the 14 flux rope CMEs in Table 2 have negative φ_{fr} values, including all 8 geoeffective ones. We currently have no explanation for why our sample of CMEs would have this preferred orientation.

We can think of no observational bias that would create this effect either. A larger sample of events should be studied to ensure this is not just a statistical fluke, but the probability of 12 or more of 14 events having the same φ_{fr} sign by chance is only 1.3%, and the probability of all eight geoeffective CMEs having the same φ_{fr} sign is only 0.8%.

In the absence of stereoscopic imaging from a mission like STEREO, one approach to estimating CME trajectory shortly after eruption is simply to assume the CME expands radially from its source region. We can use our sample of events to assess the accuracy of such an approximation. Comparing the source locations and CME trajectories in Table 2, we find that our eight geoeffective CMEs end up an average of 19° from the trajectories expected from the source region. The largest deflection (44°) is for the March 2012 event, where the geoeffective CME2 is likely deflected by the faster CME1, which erupts only an hour earlier. However, coronal deflections are also possible even in the absence of other CMEs. Coronal topology can affect CME trajectory [*Gui et al*., 2011; *Shen et al*., 2011; *Liewer et al*., 2015], and we invoke this subsequently to explain most apparent deflections close to the Sun. *Kay et al*. [2013, 2015] have recently studied the issue of CME deflection in detail.

Because of the highly nonradial nature of the coronal field inside the source surface (taken to be at $r = 2.5\ R_\odot$), CMEs can be deflected from their source region in the direction where the coronal field decreases most steeply and thus toward the successive tops of the overlying loops. In general, every CME may be considered to originate from underneath a coronal streamer, of which there are two distinct kinds: those that separate coronal holes of opposite polarity and extend outward to form the heliospheric current sheet ("helmet streamers") and those that separate coronal holes of the same polarity and do not have current sheet extensions ("pseudostreamers") [see, e.g., *Wang*, 2015]. In either case, an underlying ejection tends to be channeled magnetically toward the streamer cusp. Our analysis suggests that such deflections can be the difference between a CME hitting Earth and being geoeffective, and the same CME missing Earth entirely. The September 2011 event is perhaps the best example of this, as noted at the end of section 4.2, but the October 2011 and February 2014 events are also good examples.

The divergence of reality from expectation for the March 2015 event, as well as others in our sample (e.g., the October 2011 event) questions the validity and utility of current understanding and forecasting of severe geomagnetic storms [e.g., *Kamide and Kusano*, 2015]. *Kataoka et al*. [2015] propose that the surprising geoeffectiveness of the March 2015 event is due in part to a high speed stream the follows the CME at Earth, leading to enhancements in wind speed, magnetic field, and density. Studies of extreme events using conventional heliospheric propagation models, such as were engaged for speculation about the impact of the July 2012 CME, had it been directed toward the Earth [*Baker et al*., 2013], may not realistically capture the breadth and extent of solar eruptive activity nor their potential geomagnetic, ionospheric, and technological consequences.

6. Summary

For a sample of nine strong geomagnetic storms in solar cycle 24, we have analyzed in detail the multiple observations that characterize and link each event from the Sun to the Earth. We use STEREO, LASCO, and SDO images to identify the solar sources, heliospheric morphology, and kinematics of the responsible CMEs, *Wind* observations at L1 to quantify heliospheric conditions near Earth, TEC maps to determine the consequent ionospheric impacts, and WAAS outage to assess operational consequences. A major motivation for studies of this nature is to try to identify systematic correlations that might engender improved forecasting of solar storm disruptions of the ionosphere and consequential operational impacts, though we unfortunately failed to find any clear predictive properties. Some specific results of our study are

1. Regional TEC responses to solar storms are fairly consistent, at least in the positive ionospheric storm phase, whose strength globally correlates inversely with *ap*. The five events arriving at 13:00–21:00 UT, corresponding to local daytime in North America, yielded the largest WAAS degradations, with the four events arriving outside this time range having less or no WAAS impact.
2. The *Dst* index is a much stronger indicator than *ap* of global TEC changes in the subsequent negative phase of the storm; the correlation of *Dst* and global TEC changes is highly significant even for our small sample of nine events. But there is no clear correlation between global TEC and *Dst* in the positive phase.
3. While all the events exhibit periods of negative B_z, which is generally considered crucial for geoeffectiveness, the B_z behavior is actually very diverse, some of the negative B_z periods are only a few hours. VB_z correlates

with TEC changes only in the negative storm phase; the correlation during the positive storm phase is not significant for our sample of nine events. The CME reconstruction analysis illustrates the potential difficulties in connecting a geomagnetic storm with its solar source, as in four cases (the June 2011, August 2011, October 2011, and March 2012 events); multiple CMEs have to be reconstructed to identify the true CME responsible for the storm, and the stereoscopic and heliospheric imaging capabilities of STEREO were crucial in this regard.

4. The events include at least two cases of geoeffective shock sheaths encountered at a grazing incidence angle (the September 2011 and February 2014 events), with the CME flux rope missing Earth entirely according to our reconstruction.
5. All the geoeffective CMEs are relatively fast, eruptive events but with a wide range of peak speeds (V_{peak} = 720–1888 km s^{-1}), and the correlation between speed and ionospheric impacts in either positive or negative storm phases is not significant for our sample.
6. All the geoeffective CMEs are bright enough to be easily trackable by STEREO far into the HI2 field of view, meaning these CMEs are all significantly brighter than average and therefore presumably more massive than average.
7. The eight reconstructed geoeffective CMEs all possess flux ropes with negative φ_{fr} values, indicating a northeast-southwest orientation. We currently have no explanation for why such an orientation preference might exist.
8. A wide variety of X-ray flare strengths are associated with the events, with two events associated with strong X flares (March 2011 and February 2014) and on the opposite end of the spectrum one event (October 2011) associated with no flare at all.
9. Comparing locations of surface activity with CME trajectory leads to estimates of CME deflection in the solar corona. We find an average deflection of 19° for our sample of events. The biggest deflection (44°) is for the March 2012 event and is almost certainly due to deflection by a preceding CME, but most deflections are presumably just due to overlying coronal topology. A few events in our sample (e.g., September 2011, October 2011, and February 2014) may have missed Earth entirely if they had simply expanded radially from the source region.

Appendix A: Coronal Mass Ejection Reconstruction Details and Supporting Information Movies of Individual Events

Provided in the supporting information are movies showing images from both STEREO spacecraft, cycling consecutively through COR1, COR2, HI1, and finally HI2. Each LASCO movie cycles through the C2 and C3 images. The movies also provide comparisons with synthetic images from our reconstructions, analogous to Figures 3 and 4. No movies are provided for the April 2010 event, for which an extensive analysis (including a movie) has already been published [*Wood et al*., 2011], or for the March 2015 event, which STEREO did not observe.

A1. April 2010

This was the first geoeffective event of cycle 24, and as such it attracted significant attention [*Möstl et al*., 2010; *Rouillard et al*., 2011], including a full STEREO-based reconstruction analogous to those discussed in section 4 [*Wood et al*., 2011]. In that analysis, two reconstructions were presented, one with a north-south orientation for the flux rope ("Model A") and another with an east-west orientation ("Model B"). We choose the former here to show in Figures 3, 4, and 11, as Model A fits the COR1 data better, and have an encounter time at Earth more consistent with in situ data.

A2. June 2011

Identifying the solar causes of this geomagnetic storm is challenging. As listed in Table 2, there are three successive C flares and eruptions from the Sun between UT 02:37 on 1 June and UT 07:22 on 2 June, from the same general area southeast of Sun center. The CMEs associated with these eruptions, designated CME1, CME2, and CME3, have increasing speed, such that the CMEs gradually converge in the STEREO imagery. We make full 3-D reconstructions of all three CMEs to establish which hit Earth and which are responsible for the geomagnetic storm. The COR1 and COR2 parts of the STEREO movie show the individual successive eruptions and our synthetic images of them based on our reconstructions. It is in HI1 that the three

distinct CMEs are seen to merge together as they cross the HI1 field of view. The reconstruction in Figure 11 represents a snapshot of the situation as the CMEs approach 1 AU, when they greatly overlap in the images.

We do not perceive clear shock fronts for any of the three CMEs, so the CMEs are modeled as flux ropes only. With peak speeds of 511 and 633 km s^{-1}, respectively (see Table 2), CME1 and CME2 are slow enough that shocks would not necessarily be expected close to the Sun. With a fast peak velocity of 1272 km s^{-1}, one would generally expect a shock for CME3. Perhaps, the fact that this CME is traveling through a region disturbed by the passage of the previous two CMEs inhibits formation of a clear, visible shock.

Based on our reconstruction, we ultimately conclude that CME1 and CME2 do not hit Earth, missing to the south and east. Only CME3, the fastest and largest of the three CMEs, hits Earth, and even it only grazes Earth (see Figure 12), leading to the particularly broad density peak in Figure 5. The arrival time of this peak agrees well with the observed Earth arrival time. The sample coronagraphic images in Figure 3, and the kinematic profile in Figure 14, are of CME3 only.

A3. August 2011

There are two candidate solar eruptions for this event, both associated with M flares from AR11261 northwest of Sun center (see Table 2), at 13:17 on 3 August and 03:41 on 4 August, respectively. These events were also the focus of a study by *Lee et al*. [2015]. The two eruptions, denoted CME1 and CME2 occur about 14 h apart, but with a peak speed of 2133 km s^{-1} CME2 is faster than CME1, which reaches only 1358 km s^{-1}. The faster CME2 therefore appears to catch up with CME1 in the HI2-A field of view. (This is best seen in the STEREO movie of the event provided in the supporting information of this article.) We reconstruct both CMEs to establish which is the cause of the geomagnetic storm. The two CMEs have very similar appearances in the images, particularly in the LASCO data. Thus, the reconstructed CME structures shown in Figures 11 and 12 are very similar.

We ultimately attribute the geomagnetic storm primarily to CME1. According to our reconstruction, both the shock and flux rope of CME1 hit Earth, with our shock arriving a few hours earlier than actually observed (see Figure 5). Despite the apparent merger of the two CME fronts in HI2-A, we perceive CME2 as still trailing behind CME1 as the CMEs approach 1 AU, as shown in Figures 11 and 12, so CME2 reaches 1 AU a little too late to be the geoeffective event. However, our CME2 reconstruction does at least have the CME2 shock hitting Earth eventually. We see no clear indication in the in situ data that there are two distinct CME encounters (see Figure 5). Does the CME2 shock in practice essentially dissipate in the midst of the CME1 ejecta, meaning that it truly is only CME1 that hits Earth? Or is the full in situ signature of this event a complicated product of a combination of CME1 and CME2? We favor the former interpretation, as our CME2 reconstruction has the flux rope just missing Earth to the west, but this conclusion is debatable. In any case, it is CME1 that is displayed in Figure 3 and Figure 14 as representative of the geoeffective event.

A4. September 2011

The event began on the Sun at 12:33 UT on 24 September with an M7.1 flare from active region AR11302. The source active region was at a location of N4E57 relative to the Sun-Earth line. The source region and CME trajectory are therefore both well east of the Sun-Earth line, though the CME is directed 16° closer to Earth in longitude than if the CME had expanded radially from the source region.

For the 24 September 2011 CME that we identify as the source of the 26 September 2011 geomagnetic storm, STEREO-B provides the best vantage point for tracking the CME from the Sun to 1 AU. (The STEREO movie of the September 2011 CME available in the supporting information most clearly shows the CME front being tracked from the Sun to 1 AU.) The appearance of the 24 September 2011 CME in white light images can be interpreted as consisting of two components: a bright central driver and a fainter shock front. The two components are apparent in the COR2 images in Figure 3. The synthetic images shown below the actual COR2 images provide a guide to how the CME's appearance is divided into a roughly circular shock front, with a brighter loop-shaped driver embedded inside it.

A5. October 2011

Three boxes are shown for the October 2011 event in Figure 15, as there are three CMEs that erupt from three different regions, which appear to ultimately merge together in the HI1 field of view. In chronological order, the three CMEs are denoted CME1, CME2, and CME3 in Table 2. Figure 4 shows eight representative images of

the three CMEs in chronological order, with the three CMEs identified. Note that in the COR2-A image there is yet another CME marked "Other CME," which is directed in the north polar direction. This CME comes nowhere near the ecliptic plane and therefore evades the fields of view of STEREO's heliospheric imagers. Therefore, we do not try to model its structure. In the final HI2-A image in Figure 4, the three CMEs are blended to the extent that they are essentially indistinguishable.

In our reconstruction in Figures 11 and 12, it is CME2 that is responsible for the geomagnetic storm. The slow CME1 ($V_{peak} = 428$ km s^{-1}) is directed entirely south of the ecliptic plane and is therefore not visible in the ecliptic plane slice shown in Figure 12. The fast CME3 ($V_{peak} = 986$ km s^{-1}) is directed too far west to impact Earth. This is the only one of the three events with a clear, visible shock in front of it in the images and is therefore the only one modeled with such a shock in the reconstruction (see Figure 11). The lack of a visible shock in images near the Sun does not preclude one from developing later during a CME's interplanetary journey. Despite the appearance of merged CME fronts in HI1 and HI2 images (see Figure 4), Figure 11 demonstrates that the flux rope cores of the three CMEs do not actually overlap in 3-D space.

The kinematics of this CME have previously been studied by *Möstl et al*. [2014]. This is easily the slowest of the eight geoeffective CMEs studied here, as shown explicitly in Figure 14. The observed Earth arrival time in Figure 5 is about 5 h earlier than the reconstruction's predicted arrival time, but the agreement may actually be better than this. The reconstruction of CME2 only includes the CME flux rope and not any shock or shock sheath that develops in front of the CME during its interplanetary journey. The first part of the density peak seen on 24 October in Figure 5 may be associated with just such a shock and shock sheath. The observed velocity agrees well with that of the reconstruction.

A6. March 2012

This is another challenging event to interpret, with two candidate CMEs. As noted in Table 2, AR11429 produced two distinct, strong X flares within about an hour of each other early on 7 March. These two flares are accompanied by two distinct CMEs, CME1 and CME2, respectively. The faster and larger CME1 ($V_{peak} = 2896$ km s^{-1}) is much brighter in images, making it difficult to distinguish the smaller, slower CME2 ($V_{peak} = 1888$ km s^{-1}) embedded within CME1, particularly in the LASCO data. It is only in movies that the distinct kinematics of CME2 separate it from the larger CME1 structure in which it appears embedded. (See the movies available in the supporting information of this article.)

In our reconstruction of these two CMEs shown in Figures 11 and 12, only CME1 is modeled with a shock front ahead of the flux rope driver, as only CME1 clearly has a visible shock ahead of it near the Sun. However, at later times the CME1 shock could be interpreted as being a combined shock of both CMEs, as it mostly envelopes both eruptions. With CME1 being directed well north of the ecliptic, only a sliver of the southern leg of the CME1 flux rope is visible in Figure 12. The CME1 flux rope is therefore not interpreted as hitting Earth. The shock does, however, and we believe it is the CME1 shock that is responsible for the initial density increase seen at 12:00 UT on day 68 (8 March) in Figure 5. This is too early for the geomagnetic storm, though. At about 21:00 UT the density decreases dramatically, followed by another density increase at 1:00 UT on day 69 (9 March). It is this density increase that we deemed the arrival time in Table 1, and there is immediately afterward an extended period of negative B_z that is clearly responsible for the subsequent geomagnetic storm. We associate this with the arrival of the CME2 flux rope.

A7. October 2013

Table 2 lists a weak C1.2 flare associated with this event, but it is really a large filament eruption that truly defines the surface activity associated with the geoeffective CME. The erupting filament/prominence is very bright in the white light images of the CME from STEREO and SOHO/LASCO, particularly in the COR2-A image in Figure 3. This is a rare example of a prominence eruption that can be followed by STEREO all the way into the HI2 field of view, though it is not quite as impressive as the two cases studied by *Wood et al*. [2016]. This prominence nicely outlines the bottom of the flux rope that we use to model the CME ejecta. Our reconstruction also includes a visible shock ahead of the flux rope, as shown in Figures 11 and 12. The CME, which reaches a peak velocity of 1229 km s^{-1}, is directed toward N15W17 relative to the Sun-Earth line (see Table 2). This reconstruction suggests that only the shock hits Earth, but the flux rope just barely misses (see Figure 12), so we would not rule out the CME ejecta hitting Earth as well. Figure 5 shows that the arrival time and velocity profiles predicted by the reconstruction agree well with observations at 1 AU.

A8. February 2014

This event is reminiscent of the September 2011 event described above, with the flare and associated CME both well to the east of the Sun-Earth line. The primary surface activity associated with the event is a strong X4.9 flare in AR11990 at the east limb of the Sun (see Figure 15). The CME is modeled with the usual flux rope plus shock structure, with the results shown in Figures 3 and 11. The CME, which reaches a peak velocity of 1508 km s^{-1}, is directed toward S20E67 relative to the Sun-Earth line (see Table 2), so the flux rope comes nowhere near Earth. Earth only receives a grazing impact from the west side of the CME shock, as in the September 2011 event. With the event not being a clear halo CME in LASCO images (see Figure 3), it would have been difficult to confidently forecast an impact at Earth at all for this event, let alone a geoeffective one.

A9. March 2015

By 2015, the spacecraft were behind the Sun, limiting contact with Earth, meaning that in 2015 STEREO did not provide the imaging constraints necessary for the kind of analysis that we describe in this section. For this reason, we are unable to reconstruct the March 2015 event like the others in our sample, explaining why this event is excluded in Figure 3.

Acknowledgments

We sincerely thank two anonymous referees for providing insightful comments that significantly improved the paper. This research has made use of solar measurements archived at NOAA's Space Weather Prediction Center (http://www.swpc.noaa.gov) and geomagnetic and ionospheric data archived at the National Geophysical Data Center (http://www.ngdc.noaa.gov) and NASA's Coordinated Data Analysis Web (http://cdaweb.gsfc.nasa.gov). *Dst* indices are at http://wdc.kugi.kyoto-u.ac.jp/dst_provisional/201310/. Information about WAAS was obtained from the William J. Hughes FAA Technical Center's WAAS site (http://www.nstb.tc.faa.gov). This research was supported by funding from NASA and the Chief of Naval Research. We appreciate discussions with colleagues of NRL's ISES research initiative.

References

Akala, A. O., A. B. Rabiu, E. O. Somoye, E. O. Oyeyemi, and A. B. Adeloye (2013), The response of African equatorial GPS-TEC to intense geomagnetic storms during the ascending phase of solar cycle 24, *J. Atmos. Sol. Terr. Phys.*, *98*, 50–62, doi:10.1016/j.jastp.2013.02.006.

Araujo-Pradere, E. A., T. J. Fuller-Rowell, and P. S. J. Spencer (2006), Consistent features of TEC changes during ionospheric storms, *J. Atmos. Sol. Terr. Phys.*, *68*, 1834–1842, doi:10.1016/j.jastp.2006.06.004.

Baker, D. N., X. Li, A. Pulkkinen, C. M. Ngwira, M. L. Mays, A. B. Galvin, and K. D. C. Simunac (2013), A major solar eruptive event in July 2012: Defining extreme space weather scenarios, *Space Weather*, *11*, 585–591, doi:10.1002/swe.20097.

Balan, N., K. Shiokawa, Y. Otsuka, T. Kikuchi, D. Vijaya Lekshmi, S. Kawamura, M. Yamamoto, and G. J. Bailey (2010), A physical mechanism of positive ionospheric storms at low latitudes and midlatitudes, *J. Geophys. Res.*, *115*, A02304, doi:10.1029/2009JA014515.

Borries, C., J. Berdermann, N. Jakowski, and V. Wilken (2015), Ionospheric storms—A challenge for empirical forecast of the total electron content, *J. Geophys. Res. Space Physics*, *120*, 3175–3186, doi:10.1002/2015JA020988.

Bothmer, V., and R. Schwenn (1998), The structure and origin of magnetic clouds in the solar wind, *Ann. Geophys.*, *16*, 1–24, doi:10.1007/s00585-997-0001-x.

Brueckner, G. E., et al. (1995), The Large Angle Spectroscopic Coronagraph (LASCO), *Sol. Phys.*, *162*, 357–402, doi:10.1007/BF00733434.

Buonsanto, M. J. (1999), Ionospheric storms—A review, *Space Sci. Rev.*, *88*, 563–601, doi:10.1023/A:1005107532631.

Burlaga, L. F. (1988), Magnetic clouds and force-free fields with constant alpha, *J. Geophys. Res.*, *93*, 7217–7224, doi:10.1029/JA093iA07p07217.

Cannon, P. S. (2009), Mitigation and exploitation of the ionosphere: A military perspective, *Radio Sci.*, *44*, RS0A20, doi:10.1029/2008RS004021.

Chen, J., R. A. Howard, G. E. Brueckner, R. Santoro, J. Krall, S. E. Paswaters, O. C. S. Cyr, R. Schwenn, P. Lamy, and G. M. Simnett (1997), Evidence of an erupting magnetic flux Rope: LASCO coronal mass ejection of 1997 April 13, *Astrophys. J.*, *490*, L191–L194, doi:10.1086/311029.

Cliver, E. W., and W. F. Dietrich (2013), The 1859 space weather event revisited: Limits of extreme activity, *J. Space Weather Space Clim.*, *3*, A31, doi:10.1051/swsc/2013053.

Datta-Barua, S., T. Walter, G. S. Bust, and W. Wanner (2014), Effects of solar cycle 24 activity on WAAS navigation, *Space Weather*, *12*, 46–63, doi:10.1002/2013SW000982.

Davies, J. A., C. H. Perry, R. M. G. M. Trines, R. A. Harrison, N. Lugaz, C. Möstl, Y. D. Liu, and K. Steed (2013), Establishing a stereoscopic technique for determining the kinematic properties of solar wind transients based on a generalized self-similarly expanding circular geometry, *Astrophys. J.*, *777*, 167, doi:10.1088/0004-637X/777/2/167.

Delaboudiniere, J.-P., et al. (1995), EIT: Extreme-ultraviolet imaging telescope for the Soho Mission, *Sol. Phys.*, *162*, 291–312, doi:10.1007/BF00733432.

Emmert, J. T., S. E. McDonald, D. P. Drob, R. R. Meier, and J. M. Picone (2014), Attribution of interminima changes in the global thermosphere and ionosphere, *J. Geophys. Res. Space Physics*, *119*, 6657–6688, doi:10.1002/2013JA019484.

Eyles, C. J., et al. (2009), The heliospheric imagers onboard the STEREO mission, *Sol. Phys.*, *254*, 387–445, doi:10.1007/s11207-008-9299-0.

Ferguson, D. C., S. P. Worden, and D. E. Hastings (2015), The space weather threat to situational awareness, communications, and positioning systems, *IEEE Trans. Plasma Sci.*, *43*(9), 3086–3098, doi:10.1109/TPS.2015.2412775.

Fuller-Rowell, T. J., M. V. Codrescu, R. J. Moffett, and S. Quegan (1994), Response of the thermosphere and ionosphere to geomagnetic storms, *J. Geophys. Res.*, *99*, 3893–3914, doi:10.1029/93JA02015.

Gibson, S. E., and B. C. Low (1998), A time-dependent three-dimensional magnetohydrodynamical model of the coronal mass ejection, *Astrophys. J.*, *493*, 460–473, doi:10.1086/305107.

Gonzalez, W. D., J. A. Joselyn, Y. Kamide, H. W. Kroehl, G. Rostoker, B. T. Tsurutani, and V. M. Vasyliunas (1994), What is a geomagnetic storm?, *J. Geophys. Res.*, *99*, 5771–5792, doi:10.1029/93JA02867.

Gopalswamy, N., S. Yashiro, H. Xie, S. Akiyama, and P. Mäkelä (2015), Properties and geoeffectiveness of magnetic clouds during solar cycles 23 and 24, *J. Geophys. Res. Space Physics*, *120*, 9221–9245, doi:10.1002/2015JA021446.

Gui, B., C. Shen, Y. Wang, P. Ye, J. Liu, S. Wang, and X. Zhao (2011), Quantitative analysis of CME deflections in the corona, *Sol. Phys.*, *271*, 111–139, doi:10.1007/s11207-011-9791-9.

Hernández-Pajares, M., J. M. Juan, J. Sanz, R. Orus, A. Garcia-Rigo, J. Feltens, A. Komjathy, S. C. Schaer, and A. Krankowski (2009), The IGS VTEC maps: A reliable source of ionospheric information since 1998, *J. Geod.*, *83*, 263–275, doi:10.1007/s00190-008-0266-1.

Howard, R. A., et al. (2008), Sun Earth Connection Coronal and Heliospheric Investigation (SECCHI), *Space Sci. Rev.*, *136*, 67–115, doi:10.1007/s11214-008-9341-4.

Immel, T. J., and A. J. Mannucci (2013), Ionospheric redistribution during geomagnetic storms, *J. Geophys. Res. Space Physics*, *118*, 7928–7939, doi:10.1002/2013JA018919.

Kamide, Y., and K. Kusano (2015), No major solar flares but the largest geomagnetic storm in the present solar cycle, *Space Weather*, *13*, 365–367, doi:10.1002/2015SW001213.
Kane, R. P. (2005), How good is the relationship of solar and interplanetary plasma parameters with geomagnetic storms?, *J. Geophys. Res.*, *110*, A02213, doi:10.1029/2004JA010799.
Kataoka, R., D. Shiota, E. Kilpua, and K. Keika (2015), Pileup accident hypothesis of magnetic storm on 17 March 2015, *Geophys. Res. Lett.*, *42*, 5155–5161, doi:10.1002/2015GL064816.
Kay, C., M. Opher, and R. M. Evans (2013), Forecasting a coronal mass ejection's altered trajectory: ForeCAT, *Astrophys. J.*, *775*, 5, doi:10.1088/0004-637X/775/1/5.
Kay, C., M. Opher, and R. M. Evans (2015), Global trends of CME deflections based on CME and solar parameters, *Astrophys. J.*, *805*, 168, doi:10.1088/0004-637X/805/2/168.
Kilpua, E. K. J., M. Mierla, A. N. Zhukov, L. Rodriguez, A. Vourlidas, and B. Wood (2014), Solar sources of interplanetary coronal mass ejections during the solar cycle 23/24 minimum, *Sol. Phys.*, *289*, 3773–3797, doi:10.1007/s11207-014-0552-4.
Krall, J. (2007), Are all coronal mass ejections hollow flux ropes?, *Astrophys. J.*, *657*, 559–566, doi:10.1086/510191.
Larson, D. E., et al. (1997), Tracing the topology of the October 18–20, 1995, magnetic cloud with ~ 0.1–100 keV electrons, *Geophys. Res. Lett.*, *24*, 1911–1914, doi:10.1029/97GL01878.
Lean, J. L., R. R. Meier, J. M. Picone, and J. T. Emmert (2011), Ionospheric total electron content: Global and hemispheric climatology, *J. Geophys. Res.*, *116*, A10318, doi:10.1029/2011JA016567.
Lee, C. O., J. G. Luhmann, X. P. Zhao, Y. Liu, P. Riley, C. N. Arge, C. T. Russell, and I. de Pater (2009), Effects of the weak polar fields of solar cycle 23: Investigation using OMNI for the STEREO mission period, *Sol. Phys.*, *256*, 345–363, doi:10.1007/s11207-009-9345-6.
Lee, C. O., C. N. Arge, D. Odstrcil, G. Millward, V. Pizzo, and N. Lugaz (2015), Ensemble modeling of successive halo CMEs: A case study, *Sol. Phys.*, *290*, 1207–1229, doi:10.1007/s11207-015-0667-2.
Lekshmi, D. V., N. Balan, S. T. Ram, and J. Y. Liu (2011), Statistics of geomagnetic storms and ionospheric storms at low and mid latitudes in two solar cycles, *J. Geophys. Res.*, *116*, A11328, doi:10.1029/2011JA017042.
Lemen, J. R., et al. (2012), The Atmospheric Imaging Assembly (AIA) on the Solar Dynamics Observatory (SDO), *Sol. Phys.*, *275*, 17–40, doi:10.1007/s11207-011-9776-8.
Lepping, R. P., L. F. Burlaga, and J. A. Jones (1990), Magnetic field structure of interplanetary magnetic clouds at 1 AU, *J. Geophys. Res.*, *95*, 11,957–11,965, doi:10.1029/JA095iA08p11957.
Lepping, R. P., et al. (1995), The WIND magnetic field investigation, *Space Sci. Rev.*, *71*, 207, doi:10.1007/BF00751330.
Li, Y., J. G. Luhmann, B. J. Lynch, and E. K. J. Kilpua (2014), Magnetic clouds and origins in STEREO era, *J. Geophys. Res. Space Physics*, *119*, 3237–3246, doi:10.1002/2013JA019538.
Liewer, P., O. Panasenco, A. Vourlidas, and R. Colaninno (2015), Observations and analysis of the non-radial propagation of coronal mass ejections near the Sun, *Sol. Phys.*, *290*, 3343–3364, doi:10.1007/s11207-015-0794-9.
Liu, Y. D., J. G. Luhmann, N. Lugaz, C. Möstl, J. A. Davies, S. D. Bale, and R. P. Lin (2013), On Sun-to-Earth propagation of coronal mass ejections, *Astrophys. J.*, *769*, 45, doi:10.1088/0004-637X/769/1/45.
Lu, G., M. E. Hagan, K. Häusler, E. Doornbos, S. Bruinsma, B. J. Anderson, and H. Korth (2014), Global ionospheric and thermospheric response to the 5 April 2010 geomagnetic storm: An integrated data-model investigation, *J. Geophys. Res. Space Physics*, *119*, 10,358–10,375, doi:10.1002/2014JA020555.
Lugaz, N., A. Vourlidas, and I. I. Roussev (2009), Deriving the radial distances of wide coronal mass ejections from elongation measurements in the heliosphere—Application to CME-CME interaction, *Ann. Geophys.*, *27*, 3479–3488, doi:10.5194/angeo-27-3479-2009.
Lugaz, N., P. Kintner, C. Möstl, L. K. Jian, C. J. Davis, and C. J. Farrugia (2012), Heliospheric observations of STEREO-directed coronal mass ejections in 2008–2010: Lessons for future observations, *Sol. Phys.*, *279*, 497–515, doi:10.1007/s11207-012-0007-8.
Maksimovic, M., J.-L. Bougeret, C. Perche, J. T. Steinberg, A. J. Lazarus, A. F. Viñas, and R. J. Fitzenreiter (1998), Solar wind density intercomparisons in the Wind spacecraft using WAVES and SWE experiments, *Geophys. Res. Lett.*, *25*, 1265–1268, doi:10.1029/98GL00843.
Manchester, W. B., T. I. Gombosi, I. Roussev, D. L. de Zeeuw, I. V. Sokolov, K. G. Powell, G. Toth, and M. Opher (2004), Three-dimensional MHD simulation of a flux rope driven CME, *J. Geophys. Res.*, *109*, A01102, doi:10.1029/2002JA009672.
Marubashi, K. (1986), Structure of the interplanetary magnetic clouds and their solar origins, *Adv. Space Res.*, *6*, 335–338, doi:10.1016/0273-1177(86)90172-9.
Mendillo, M. (2006), Storms in the ionosphere: Patterns and processes for total electron content, *Rev. Geophys.*, *44*, RG4001, doi:10.1029/2005RG000193.
Möstl, C., and J. A. Davies (2013), Speeds and arrival times of solar transients approximated by self-similar expanding circular fronts, *Sol. Phys.*, *285*, 411–423, doi:10.1007/s11207-012-9978-8.
Möstl, C., M. Temmer, T. Rollett, C. J. Farrugia, Y. Liu, A. M. Veronig, M. Leitner, A. B. Galvin, and H. K. Biernat (2010), STEREO and Wind observations of a fast ICME flank triggering a prolonged geomagnetic storm on 5–7 April 2010, *Geophys. Res. Lett.*, *37*, L24103, doi:10.1029/2010GL045175.
Möstl, C., et al. (2014), Connecting speeds, directions and arrival times of 22 coronal mass ejections from the Sun to1 AU, *Astrophys. J.*, *787*, 119, doi:10.1088/0004-637X/787/2/119.
Mukhtarov, P., B. Andonov, and D. Pancheva (2013), Global empirical model of TEC response to geomagnetic activity, *J. Geophys. Res. Space Physics*, *118*, 6666–6685, doi:10.1002/jgra.50576.
National Research Council (2013), Solar and space physics: A science for a technological society.
Patsourakos, S., et al. (2016), The major geoeffective solar eruptions of 2012 March 7: Comprehensive Sun-to-Earth analysis, *Astrophys. J.*, *817*, 14, doi:10.3847/0004-637X/817/1/14.
Rollett, T., et al. (2014), Combined multipoint remote and in situ observations of the asymmetric evolution of a fast solar coronal mass ejection, *Astrophys. J.*, *790*, L6, doi:10.1088/2041-8205/790/1/L6.
Rouillard, A. P., et al. (2011), Interpreting the properties of solar energetic particle events by using combined imaging and modeling of interplanetary shocks, *Astrophys. J.*, *735*, 7, doi:10.1088/0004-637X/735/1/7.
Royal Academy of Engineering (2013), Extreme space weather: impacts on engineered systems and infrastructure.
Russell, C. T., J. G. Luhmann, and L. K. Jian (2010), How unprecedented a solar minimum?, *Rev. Geophys.*, *48*, RG2004, doi:10.1029/2009RG000316.
Shen, C., Y. Wang, B. Gui, P. Ye, and S. Wang (2011), Kinematic evolution of a slow CME in corona viewed by STEREO-B on 8 October 2007, *Sol. Phys.*, *269*, 389–400, doi:10.1007/s11207-011-9715-8.
Shen, C., Y. Wang, Z. Pan, B. Miao, P. Ye, and S. Wang (2014), Full-halo coronal mass ejections: Arrival at the Earth, *J. Geophys. Res. Space Physics*, *119*, 5107–5116, doi:10.1002/2014JA020001.

Sojka, J. J., M. David, R. W. Schunk, and R. A. Heelis (2012), A modeling study of the longitudinal dependence of storm time midlatitude dayside total electron content enhancements, *J. Geophys. Res.*, *117*, A02315, doi:10.1029/2011JA017000.

Space Weather Operations, Research, and Mitigation (SWORM) Task Force (2015), National space weather strategy, Natil. Sci. and Technol. Counc., Executive Off. of the President of the U. S.

Thernisien, A., A. Vourlidas, and R. A. Howard (2009), Forward modeling of coronal mass ejections using STEREO/SECCHI data, *Sol. Phys.*, *256*, 111–130, doi:10.1007/s11207-009-9346-5.

Thernisien, A. F. R., R. A. Howard, and A. Vourlidas (2006), Modeling of flux rope coronal mass ejections, *Astrophys. J.*, *652*, 763–773, doi:10.1086/508254.

Thomas, E. G., J. B. H. Baker, J. M. Ruohoniemi, L. B. N. Clausen, A. J. Coster, J. C. Foster, and P. J. Erickson (2013), Direct observations of the role of convection electric field in the formation of a polar tongue of ionization from storm enhanced density, *J. Geophys. Res. Space Physics*, *118*, 1180–1189, doi:10.1002/jgra.50116.

Tsurutani, B. T., W. D. Gonzalez, G. S. Lakhina, and S. Alex (2003), The extreme magnetic storm of 1–2 September 1859, *J. Geophys. Res.*, *108*(A7), 1268, doi:10.1029/2002JA009504.

Vourlidas, A., B. J. Lynch, R. A. Howard, and Y. Li (2012), How many CMEs have flux ropes? Deciphering the signatures of shocks, flux ropes, and prominences in coronagraph observations of CMEs, *Sol. Phys.*, *284*, 179–201, doi:10.1007/s11207-012-0084-8.

Wang, Y., C. L. Shen, S. Wang, and P. Z. Ye (2003), An empirical formula relating the geomagnetic storm's intensity to the interplanetary parameters: $-VB_z$ and Δt, *Geophys. Res. Lett.*, *30*(20), 2039, doi:10.1029/2003GL017901.

Wang, Y.-M. (2015), Pseudostreamers as the source of a separate class of solar coronal mass ejections, *Astrophys. J.*, *803*, L12, doi:10.1088/2041-8205/803/1/L12.

Wood, B. E., and R. A. Howard (2009), An empirical reconstruction of the 2008 April 26 coronal mass ejection, *Astrophys. J.*, *702*, 901–910, doi:10.1088/0004-637X/702/2/901.

Wood, B. E., C.-C. Wu, R. A. Howard, D. G. Socker, and A. P. Rouillard (2011), Empirical reconstruction and numerical modeling of the first geoeffective coronal mass ejection of solar cycle 24, *Astrophys. J.*, *729*, 70, doi:10.1088/0004-637X/729/1/70.

Wood, B. E., C.-C. Wu, A. P. Rouillard, R. A. Howard, and D. G. Socker (2012), A coronal hole's effects on coronal mass ejection shock morphology in the inner heliosphere, *Astrophys. J.*, *755*, 43, doi:10.1088/0004-637X/755/1/43.

Wood, B. E., R. A. Howard, and M. G. Linton (2016), Imaging prominence eruptions out to 1 AU, *Astrophys. J.*, *816*, 67, doi:10.3847/0004-637X/816/2/67.

Wu, C.-C., and R. P. Lepping (2002), Effects of magnetic clouds on the occurrence of geomagnetic storms: The first 4 years of Wind, *J. Geophys. Res.*, *107*(A10), 1314, doi:10.1029/2001JA000161.

Wu, S. T., M. D. Andrews, and S. P. Plunkett (2001), Numerical magnetohydrodynamic (MHD) modeling of coronal mass ejections (CMEs), *Space Sci. Rev.*, *95*, 191–213, doi:10.1023/A:1005284600631.

Zhang, S.-R., et al. (2015), Thermospheric poleward wind surge at midlatitudes during great storm intervals, *Geophys. Res. Lett.*, *42*, 5132–5140, doi:10.1002/2015GL064836.